Planck 2013 results. IX. HFI spectral response

Planck Collaboration,; Ade, P. A. R.; Aghanim, N.; Armitage-Caplan, C.; Arnaud, M.; Ashdown, M.; Atrio-Barandela, F.; Aumont, J.; Baccigalupi, C.; Banday, A. J.

Total number of authors:
218

Published in:
ArXiv Astrophysics e-prints

Publication date:
2013

Document Version
Publisher's PDF, also known as Version of record

Astronomy & Astrophysics manuscript no. HFI˙Spectral˙Bands
March 22, 2013

Planck 2013 results. IX. HFI spectral response

Planck Collaboration: P. A. R. Ade[79], N. Aghanim[54], C. Armitage-Caplan[83], M. Arnaud[66], M. Ashdown[63,6], F. Atrio-Barandela[18], J. Aumont[54], C. Baccigalupi[78], A. J. Banday[86,10], R. B. Barreiro[60], E. Battaner[87], K. Benabed[55,85], A. Benoît[52], A. Benoit-Lévy[23,55,85], J.-P. Bernard[10], M. Bersanelli[32,45], P. Bielewicz[86,10,78], J. Bobin[66], J. J. Bock[61,11], J. R. Bond[9], J. Borrill[14,80], F. R. Bouchet[55,85], F. Boulanger[54], M. Bridges[63,6,58], M. Bucher[1], C. Burigana[44,30], J.-F. Cardoso[67,1,55], A. Catalano[68,65], A. Challinor[58,63,12], A. Chamballu[66,15,54], R.-R. Chary[51], X. Chen[51], L.-Y Chiang[57], H. C. Chiang[25,7], P. R. Christensen[74,35], S. Church[82], D. L. Clements[50], S. Colombi[55,85], L. P. L. Colombo[22,61], C. Combet[68], B. Comis[68], F. Couchot[64], A. Coulais[65], B. P. Crill[61,75], A. Curto[6,60], F. Cuttaia[44], L. Danese[78], R. D. Davies[62], P. de Bernardis[31], A. de Rosa[44], G. de Zotti[41,78], J. Delabrouille[1], J.-M. Delouis[55,85], F.-X. Désert[48], C. Dickinson[62], J. M. Diego[60], H. Dole[54,53], S. Donzelli[45], O. Doré[61,11], M. Douspis[54], X. Dupac[37], G. Efstathiou[58], T. A. Enßlin[71], H. K. Eriksen[59], E. Falgarone[65], F. Finelli[44,46], O. Forni[86,10], M. Frailis[43], E. Franceschi[44], S. Galeotta[43], K. Ganga[1], M. Giard[86,10], Y. Giraud-Héraud[1], J. González-Nuevo[60,78], K. M. Górski[61,89], S. Gratton[63,58], A. Gregorio[33,43], A. Gruppuso[44], F. K. Hansen[59], D. Hanson[72,61,9], D. Harrison[58,63], S. Henrot-Versillé[64], C. Hernández-Monteagudo[13,71], D. Herranz[60], S. R. Hildebrandt[11], E. Hivon[55,85], M. Hobson[6], W. A. Holmes[61], A. Hornstrup[16], W. Hovest[71], K. M. Huffenberger[88], G. Hurier[54,68], T. R. Jaffe[86,10], A. H. Jaffe[50], W. C. Jones[25], M. Juvela[24], E. Keihänen[24], R. Keskitalo[21,14], T. S. Kisner[70], R. Kneissl[36,8], J. Knoche[71], L. Knox[26], M. Kunz[17,54,3], H. Kurki-Suonio[24,39], G. Lagache[54], J.-M. Lamarre[65], A. Lasenby[6,63], R. J. Laureijs[38], C. R. Lawrence[61], J. P. Leahy[62], R. Leonardi[37], C. Leroy[54,86,10], J. Lesgourgues[84,77], M. Liguori[29], P. B. Lilje[59], M. Linden-Vørnle[16], M. López-Caniego[60], P. M. Lubin[27], J. F. Macías-Pérez[68], B. Maffei[62], N. Mandolesi[44,5,30], M. Maris[43], D. J. Marshall[66], P. G. Martin[9], E. Martínez-González[60], S. Masi[31], S. Matarrese[29], F. Matthai[71], P. Mazzotta[34], P. McGehee[51], A. Melchiorri[31,47], L. Mendes[37], A. Mennella[32,45], M. Migliaccio[58,63], S. Mitra[49,61], M.-A. Miville-Deschênes[54,9], A. Moneti[55], L. Montier[86,10], G. Morgante[44], D. Mortlock[50], D. Munshi[79], J. A. Murphy[73], P. Naselsky[74,35], F. Nati[31], P. Natoli[30,4,44], C. B. Netterfield[19], H. U. Nørgaard-Nielsen[16], C. North[79], F. Noviello[62], D. Novikov[50], I. Novikov[74], S. Osborne[82], C. A. Oxborrow[16], F. Paci[78], L. Pagano[31,47], F. Pajot[54], D. Paoletti[44,46], F. Pasian[43], G. Patanchon[1], O. Perdereau[64], L. Perotto[68], F. Perrotta[78], F. Piacentini[31], M. Piat[1], E. Pierpaoli[22], D. Pietrobon[61], S. Plaszczynski[64], E. Pointecouteau[86,10], G. Polenta[4,42], N. Ponthieu[54,48], L. Popa[56], T. Poutanen[39,24,2], G. W. Pratt[66], G. Prézeau[11,61], S. Prunet[55,85], J.-L. Puget[54], J. P. Rachen[20,71], M. Reinecke[71], M. Remazeilles[54,1], C. Renault[68], S. Ricciardi[44], T. Riller[71], I. Ristorcelli[86,10], G. Rocha[61,11], C. Rosset[1], G. Roudier[1,65,61], B. Rusholme[51], D. Santos[68], G. Savini[76], E. P. S. Shellard[12], L. D. Spencer*[79], J.-L. Starck[66], V. Stolyarov[6,63,81], R. Stompor[1], R. Sudiwala[79], F. Sureau[66], D. Sutton[58,63], A.-S. Suur-Uski[24,39], J.-F. Sygnet[55], J. A. Tauber[38], D. Tavagnacco[43,33], L. Terenzi[44], M. Tomasi[45], M. Tristram[64], M. Tucci[17,64], G. Umana[40], L. Valenziano[44], J. Valiviita[39,24,59], B. Van Tent[69], P. Vielva[60], F. Villa[44], N. Vittorio[34], L. A. Wade[61], B. D. Wandelt[55,85,28], D. Yvon[15], A. Zacchei[43], and A. Zonca[27]

(Affiliations can be found after the references)

Received XX, 2013; accepted XX, 2013

ABSTRACT

The *Planck* High Frequency Instrument (HFI) spectral response was determined through a series of ground based tests conducted with the HFI focal plane in a cryogenic environment prior to launch. The main goal of the spectral transmission tests is to measure the relative spectral response (including the level of out-of-band signal rejection) of all HFI detectors to a known source of electromagnetic radiation individually. This was determined by measuring the interferometric output of all detection channels for radiation propagated through a continuously scanned polarizing Fourier transform spectrometer. As there is no on-board spectrometer within HFI, the ground-based spectral response experiments provide the definitive data set for the relative spectral calibration of the HFI. Knowledge of the relative variations in the spectral response between HFI detectors allows for a more thorough analysis of the HFI data. The spectral response of the HFI is used in *Planck* component separation and data analysis, this includes extraction of CO emission observed within *Planck* bands, dust emission, Sunyaev Zeldovich sources, and intensity to polarization leakage. The HFI spectral response data have also been used to provide unit conversion and colour correction analysis tools.
While previous papers have already described the pre-flight experiments conducted on the *Planck* HFI, this paper focuses on the analysis of the pre-flight spectral response measurements and the derivation of data products, e.g. band-average spectra, unit conversion coefficients, and colour correction coefficients, all with related uncertainties. Verifications of the HFI spectral response data are provided through comparisons with HFI flight data. This validation includes use of HFI Zodiacal emission observations to demonstrate out-of-band spectral signal rejection better than 10^8. The accuracy of the HFI relative spectral response data is verified through comparison of complementary bandpass based and flight-data based unit conversion coefficients and colour correction coefficients. These coefficients include those based upon HFI observations of CO, dust, and Sunyaev-Zeldovich emission. General agreement is observed between the ground-based spectral characterization of HFI and corresponding in-flight observations, within the quoted uncertainty of each; explanations are provided for any discrepancies.

Key words. Astronomical instrumentation, methods and techniques – Instrumentation: detectors – Instrumentation: photometers – Space vehicles: instruments – Cosmology: observations – cosmic background radiation

1. Introduction

This paper, one of a set associated with the 2013 release of data from the *Planck*[1] mission (Planck Collaboration I 2013),

*Corresp. author: L.D.Spencer, Locke.Spencer@astro.cf.ac.uk

[1] *Planck* (http://www.esa.int/Planck) is a project of the European Space Agency (ESA) with instruments provided by two sci-

describes the determination and verification of the *Planck* High Frequency Instrument (HFI) spectral response. As the HFI employs a series of broad-band photometric receivers, an accurate understanding of the relative spectral response of each detector within a frequency channel, and that of each frequency channel within the instrument, is important in data processing and analysis (Planck Collaboration VI 2013); this is particularly important for *Planck* component separation (Planck Collaboration XII 2013) where the magnitude of foreground components is much greater than the uncertainties associated with the cosmic microwave background (CMB) signals.

The *Planck* High Frequency Instrument (HFI) spectral response was determined through a series of ground based tests conducted with the HFI focal plane in a cryogenic environment prior to launch. One of the main goals in pre-flight calibration testing was to measure the relative spectral response (including the level of out-of-band signal rejection) of all HFI detectors to a known source of electromagnetic (EM) radiation individually. This was determined by measuring the interferometric output of all detection channels for radiation propagated through a continuously scanned polarizing Fourier transform spectrometer (FTS). As there is no on-board spectrometer within HFI, the ground-based spectral response experiments provide the definitive spectral calibration of HFI. Pre-flight component level spectral characterization testing is described in detail in Ade et al. (2010). The pre-flight system level spectral characterization testing is described in detail in Pajot et al. (2010). This paper will discuss the testing itself as needed to provide context, but will primarily concentrate on the spectral characterization measurements, their analysis, and their utility within the HFI consortium and the *Planck* legacy data archive. Additional details of the HFI pre-flight calibration are found in Rosset et al. 2010, Lamarre et al. 2010, and Maffei et al. (2010). The average spectrum for each of the HFI bands is illustrated in Figure 1 (see Sect. 3.1 for details).

An accurate understanding of the spectral response of HFI is critical in HFI data processing and analysis. Information derived from the spectral calibration is important in many aspects of component separation (Planck Collaboration XII 2013). Unit conversion factors and colour corrections, which are important when dealing with signals of varying spectral profiles within a photometric channel, are derived for HFI using the transmission spectra. Spectral mismatch between detectors within a given band must be understood in order to accurately interpret multi-detector averages and differences that otherwise yield systematic errors and increased uncertainty in data products. This is especially important in the evaluation of weak components including polarized signal.

This paper presents the propagation of the raw spectral characterization data through its processing and analysis to yield detector level spectral response data in Sect. 2. Sect. 3 then describes the analysis of the detector spectral transmission data to provide advanced spectral data products such as band-average spectra and unit conversion / colour correction coefficients. Sect. 4 presents the evaluation of the HFI spectral response and data products through comparisons with flight data. This includes comparisons with HFI observations of Zodiacal light (Planck Collaboration XIV 2013), CO emission (Planck Collaboration XIII 2013), Sunyaev-Zeldovich sources (Planck Collaboration XXVIII 2013, Planck Collaboration XXIX 2013, and Planck Collaboration XXI 2013), and dust emission (Planck Collaboration 2013, Planck Collaboration XVII 2011, and Planck Collaboration XIX 2011).

entific consortia funded by ESA member states (in particular the lead countries France and Italy), with contributions from NASA(USA) and telescope reflectors provided by a collaboration between ESA and a scientific consortium led and funded by Denmark.

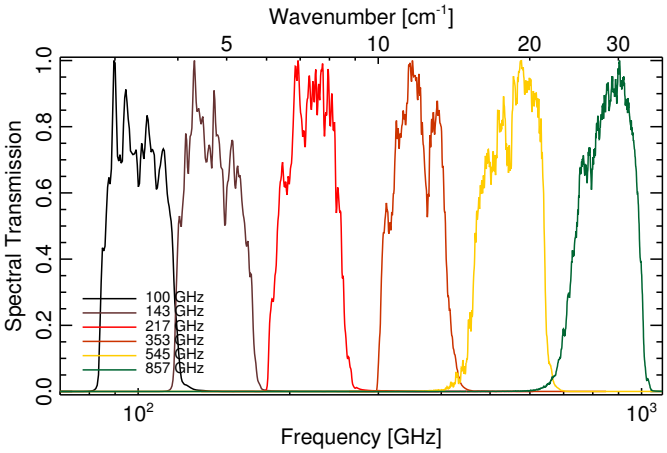

Fig. 1. Band-average spectral transmission for each of the HFI frequency channels.

Details of the spectral response of the *Planck* LFI instrument may be found in Planck Collaboration II (2013) and in Zonca et al. (2009). Further details on technical aspects of the HFI spectral response data are also available in the *Planck* Explanatory Supplement (Planck Collaboration ES 2013).

2. Measurements

This section outlines the pre-flight data collected allowing the HFI spectral response determination. The processing of the recorded data is outlined, and the resultant spectra are presented.

2.1. Spectral Response Data Collection

The *Planck* HFI detector spectral response data were measured using a broadband mercury arc lamp radiation source, a polarizing FTS, an integrating sphere, and a rotating filter wheel, all coupled with the HFI focal plane in its evacuated cryostat. A reference bolometer (at approx. 4 K) was mounted within the integrating sphere as an external measure of the radiation incident on HFI (see Fig. 3, Pajot et al. 2010). With this configuration, the entire HFI focal plane and the reference bolometer were exposed to the FTS modulated spectral signal synchronously. The ratio of the HFI detector spectra with the reference bolometer spectra provides a relative spectral response with the systematics due to the test configuration removed. The HFI spectral response measurements were collected during June and July of 2006 at the Institut d'Astrophysique Spatiale (IAS) laboratories in Orsay, France. For each HFI detector, roughly 100 interferograms were recorded with consistent scan parameters to allow a spectral resolution of approximately 0.5 GHz and a Nyquist frequency (Nyquist (1928) and Shannon (1948)) of approximately 12 000 GHz in the resultant spectra. The rotating filter wheel was placed before the entrance to the integrating sphere with two settings used in these observations (Pajot et al. 2010). A 10 cm^{-1}(approx. 300 GHz) [2] low-pass edge (LPE) filter was used for observations of the 100 – 217 GHz detectors while a 36 cm^{-1}(approx. 11 000 GHz) LPE filter was used for the 353 –

[2] The term wavenumber will be used to refer to units of cm^{-1}.

857 GHz observations. The LPE filtering external to HFI and the integrating sphere allowed better performance of the reference bolometer over the low frequency channel spectral range, as will be shown below. Further details of the experimental setup, including diagrams of the FTS, integrating sphere, and HFI focal plane locations, are found in Pajot et al. (2010). Additional relevant information is also found in Ade et al. (2010).

There were two significant additional tests in the derivation of the HFI detector spectral response beyond the scope of the IAS HFI FTS measurements. Optical efficiency experiments, also conducted at IAS, provide optical efficiency estimates for each HFI detector. When coupled with the FTS spectra this allows an estimate of the absolute spectral transmission. More details on the optical efficiency tests are in Catalano (2008); Catalano et al. (2006). Additional filter measurements were recorded in the AIG test facility at Cardiff during filter stack production (Ade et al. 2010). These measurements extend the IAS FTS spectral measurements far beyond the HFI spectral passband up to approximately 20 THz. The independent measure of the filter stack transmission is used for a portion of the HFI detector spectral transmission for regions of the spectrum where it is deemed to be of better quality then the IAS FTS measurements (i.e., for frequencies outside of the HFI band edge filter cut-off). The filter stacks for each of the frequency bands are comprised of 5 filters. There is an additional low frequency cut-on filter for the 545 and 857 GHz bands as the waveguide cut-on is too low for the desired multi-mode performance (Ade et al. 2010 and Murphy et al. 2010).

2.2. Spectral Response Data Processing

The raw detector signals were combined with a bolometer model (Holmes et al. 2008, Lamarre et al. 2010, and Planck HFI Core Team 2011) to both convert the signal into physical units and perform a detector nonlinearity correction (Naylor et al. 2009). The recorded interferograms were processed and Fourier transformed individually (Bell 1972 and Davis et al. 2001), including phase correction (Forman et al. 1966 and Brault 1987) and apodization (Naylor & Tahic 2007). The resultant spectra were then averaged together to provide a mean and standard deviation for every independent spectral data point. Similar analysis was conducted for the reference bolometer measurements. The ratio of each detector average spectrum against the corresponding reference bolometer average spectrum was taken to obtain the relative spectral transmission. Fig. 2 demonstrates an example set of raw and average spectra for the HFI 100 GHz 1a detector. The signal-to-noise (S/N) ratios for the average spectra for each HFI detector and the relevant spectral region of the reference bolometer spectra are shown in Fig. 3. In terms of the noise of the HFI detector relative transmission spectra, the reference bolometer is the limiting case, especially for the 100 GHz detectors. It is important to note, however, that each HFI detector spectrum within a given frequency band is divided by the same reference bolometer spectrum. Therefore, the *relative* uncertainty between HFI detectors is indicated by the HFI-only marks of Fig. 3, even though the *absolute* uncertainty is dictated by the limiting S/N of the reference bolometer. The detector relative transmission spectra are normalized to have a maximum value of unity, with the optical efficiency test results (Catalano 2008) providing a multiplicative term to obtain the absolute spectral response, i.e., the product of the normalized spectral response and the optical efficiency factor provides an estimate of the absolute spectral response of a given detector. As the reference bolometer accepts 2π sr. of incident radiation within the integrating sphere, the relative transmission spectrum for each HFI detector is also throughput [3] normalized by virtue of the reference bolometer ratio.

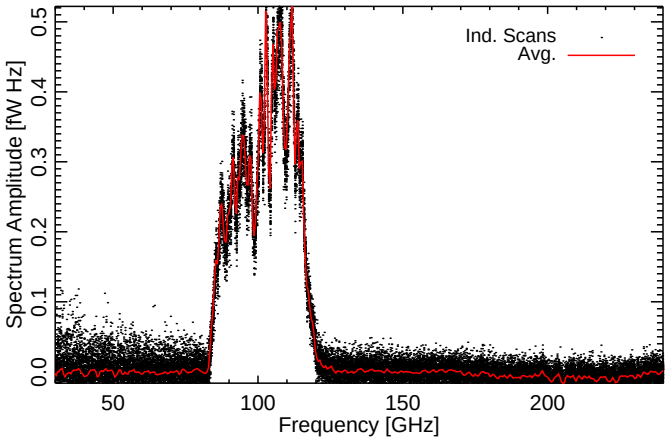

Fig. 2. Sample bolometer spectra from HFI 100 GHz detector 1a. The black data represent individual spectra while the colored data represent the average of the approx. 100 individual spectra.

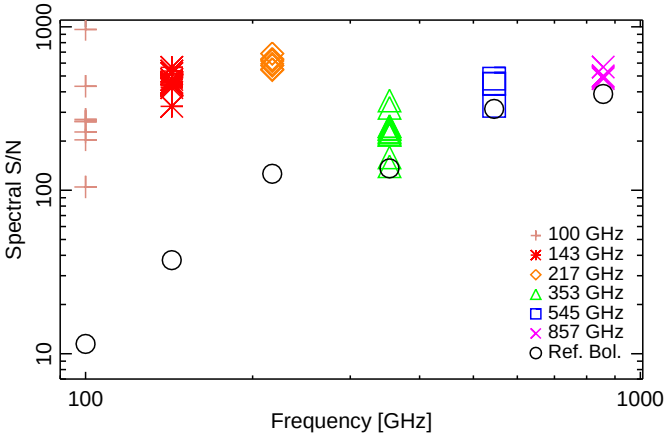

Fig. 3. HFI detector spectral S/N for the scan-averaged HFI detector spectra prior to taking the ratio with the scan-averaged reference spectra. Also shown is the S/N for the scan-averaged reference bolometer spectra over the same spectral region.

Once the detector and reference spectra ratios have been obtained, the out-of-band spectral regions are modified to improve the overall data quality. A waveguide model is used for the low frequency pre-cut-on region and the component level filter stack spectra are used for the post-cut-off spectral regions (see Ade et al. (2010) for more details). For the 545 and 857 GHz channels, the component level filter spectra are also used in conjunction with the waveguide model for the pre-cut-on spectral region. Fig. 4 illustrates an example composite spectrum showing the relative FTS spectrum, the waveguide model, the component level filter spectra, and the corresponding spectral transition regions where the external spectra are spliced onto the in-band spectrum.

At this stage, the frequency sampling for a given detector may be slightly different than those within the same frequency channel as each detector signal is processed independently. To allow easier intra-channel comparisons, all spectra are then interpolated onto a common frequency grid within each of the HFI

[3] Throughput, i.e., $A\,\Omega$, is defined as the area - solid angle product of a diffraction limited system (Born & Wolf 1999).

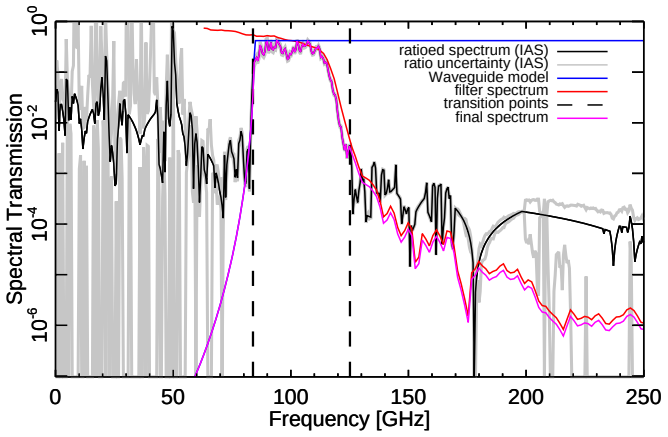

Fig. 4. Example ratioed spectrum (black), filter spectrum (red), and waveguide model (blue) for bc00 – 100 GHz 1a. The transition frequencies are shown by the vertical dashed lines. The out-of-band transmission is a conservative over-estimates as the ratioed spectrum is scaled by the optical efficiency prior to out-of-band grafting of the waveguide model and filter data.

frequency channels. As all measurements within a frequency channel are conducted synchronously, and all detectors are referenced against the same reference bolometer, uncertainties introduced as a result of the common frequency interpolation are expected to be negligible. The largest differences occur as a result of differences in band-edge location, and thus the transition frequency when the component level filter spectra (at a lower spectral resolution) are used in place of the IAS spectra. The common frequency sampling adopted attempts to mitigate the inclusion of additional spectral uncertainty by selecting the limiting case within a frequency band, e.g., the lowest filter-spectrum transition point is selected to avoid the interpolation increasing the localized spectral resolution of any detector spectra. This may result in a minor degradation of the spectral resolution for some detectors, but does not result in presenting data at a higher spectral resolution than it was originally measured with.[4]

Regions of the HFI spectral range with sensitivity to CO emission are identified (Jet Propulsion Laboratory 2004). To assist with the use of the HFI spectral response data with HFI CO studies (see Planck Collaboration XIII (2013)), the signal in the HFI CO spectral regions (see Table 1) is interpolated by a factor of 10 using the FTS instrument line shape (ILS) (Connes 1961). Although the data are presented at higher resolution, the native spectral resolution of the underlying data does not increase with this interpolation, i.e., the number of independent data points is not increased and the FTS instrument line-width remains the same. While this interpolation provides a more accurate estimate of the spectral transmission within these regions than, e.g., linear interpolation, it is important to note that these data do not correspond to independent sampled frequency data points. Thus, a flag column has been added to the spectral transmission profile data files to indicate whether a given data point originates from the actual data, or is a result of the ILS-based interpolation. The interpolation regions have been extended to include the frequency range of other CO isotopes (i.e., CO, ^{13}CO, C^{17}O, and C^{18}O) over a range of radial velocities (i.e., $\pm 300 \mathrm{km\,s^{-1}}$). The original data points within the over-sampled region have been preserved, so a flag filter on the data will restore the independent data points easily.

[4] The CO interpolation, discussed below, is an exception to this.

Table 1. HFI regions of CO rotational transmission

Band [GHz]	CO transition ($J_{\rm upper} \rightarrow J_{\rm lower}$)	$\nu_{\rm CO}$ [GHz]	over-sampled region [GHz]
100	$1 \rightarrow 0$	115.2712018	109.67 – 115.39
217	$2 \rightarrow 1$	230.5380000	219.34 – 230.77
353	$3 \rightarrow 2$	345.7959899	329.00 – 346.15
545	$4 \rightarrow 3$	461.0407682	438.64 – 461.51
545	$5 \rightarrow 4$	576.2679305	548.28 – 576.85
857	$6 \rightarrow 5$	691.4730763	657.89 – 692.17
857	$7 \rightarrow 6$	806.6518060	767.48 – 807.46
857	$8 \rightarrow 7$	921.7997000	877.04 – 922.73
857	$9 \rightarrow 8$	1036.9123930	986.57 – 1037.95

2.3. Spectral Response Data Products

The HFI detector spectral response data products are available within the database instrument model (see Planck Collaboration ES (2013)) and within the *Planck* legacy archive (PLA). The data is comprised of the spectral frequency in units of both GHz and $\mathrm{cm^{-1}}$, the normalized spectral response (with its associated uncertainty), a CO interpolation flag, and meta-data including waveguide and filter transition regions, optical efficiency, and date/version information. The spectral normalization is such that the maximum value of any given spectrum is unity. An estimate of the absolute spectral transmission is obtained through the product of the optical efficiency parameter and the normalized spectrum for a given detector or frequency band (see Planck Collaboration ES (2013) for further details). Figs. 5 – 10 present the spectral response for each of the HFI detectors. Several diagnostic parameters are determined for each HFI detector spectrum (and the band-average and detector sub-set spectra, see Sect. 3.1 and Table 4). These parameters include the cut-on and cut-off frequency, the effective bandwidth, the central frequency, various effective frequencies, and the optical efficiency, all of which are defined below.

The following definitions are used in the evaluation of the spectral transmission profiles for the HFI detectors:

- *Cut-on, ν_{on}:* The Cut-on frequency defines where the spectral band or the high-pass filter frequency dependence goes from the minimum to the maximum value. The cut-on position of the filter is usually referred to as the position in frequency (or wavenumber) space where the smooth varying function in question reaches half of the maximum power.
  In the most general case, this definition encounters a problem when dealing with spectra that have small peaks and can oscillate above and below the half-power mark in getting to the maximum in band power. Moreover the maximum in band power can be a peak value, an average value, or the band itself can have a "sloped" shape that biases the actual definition of half-maximum level. The cut-on frequency in this work is defined as the lowest frequency occurrence of half-maximum amplitude.
- *Cut-off, ν_{off}:* Similar arguments apply to the cut-off as for the cut-on. The cut-off frequency in this work is defined as the highest frequency occurrence of half-maximum amplitude.
- *Bandwidth, $\Delta\nu$:* The FWHM of the optical band, given by

$$\Delta\nu = \nu_{\rm off} - \nu_{\rm on} \quad . \tag{1}$$

– *Central Frequency, ν_{cen}:* The central frequency is defined as the average of ν_{on} and ν_{off}. A more useful parameter, however, is the *effective frequency*, ν_{eff}.
– *Effective frequency*, ν_{eff}: Alternatively the effective frequency is usually defined by weighing the spectra by the frequency itself and is analogous to the most-probable frequency and is given by

$$\nu_{eff} = \frac{\int \nu\tau'(\nu)d\nu}{\int \tau'(\nu)d\nu} \quad , \tag{2}$$

where $\tau'(\nu)$ is the spectral transmission including the optical efficiency term ε.
– *Integrated optical efficiency*, ε_{Int}: The integrated optical efficiency is obtained by integrating the spectral transmission across the entire measured frequency range, and dividing by the detector bandwidth as follows

$$\varepsilon_{Int} = \frac{\epsilon \int \tau(\nu)d\nu}{\Delta\nu} \quad , \tag{3}$$

where ϵ is the relative optical efficiency discussed in Sect. 2.2 above, ε_{Int} is the integrated optical efficiency introduced here, $\tau(\nu)$ is the normalized spectral transmission, and $\Delta\nu$ is the bandwidth as described in Eq. 1 above.
– *Spectral index effective frequencies*, $\nu_{\alpha,eff}$: As in the effective frequency case, this is equivalent to weighing the transmission spectrum by the frequency while including a different spectral index, α. The effective frequency including spectral index is given by

$$\nu_{\alpha,eff} = \frac{\int \nu\left(\frac{\nu}{\nu_c}\right)^{\alpha} \tau'(\nu)d\nu}{\int \left(\frac{\nu}{\nu_c}\right)^{\alpha} \tau'(\nu)d\nu} \quad , \tag{4}$$

where ν_c is the nominal band reference frequency. [5]

There is an important distinction between ϵ and ε_{Int} in that the former is a scaling term, which accompanies the normalized transmission spectra (and is meaningless on its own), and the latter is intended to represent an effective optical efficiency over the specified bandwidth, i.e., an equivalent spectral rectangle/tophat function.

In addition to the individual detector spectra, several other data products have been prepared for distribution. These include band-average spectra (see Sect. 3.1, and also Table 4), unit conversion / colour correction coefficients (see Sect. 3.2), and unit conversion/colour correction, UcCC, software scripts to accompany HFI data (see Planck Collaboration ES (2013)). These data products are discussed in the following sections. Tables 2 and 3 report the parameters derived from the HFI detector spectral transmission profile data products as defined above, for the HFI band-average spectra; similar results for all HFI detectors are available in Planck Collaboration ES (2013). The spectral indices chosen for Table 3 correspond to the IRAS SED ($\alpha = -1$), a planetary SED ($\alpha = 2$), and a dust SED ($\alpha = 4$).

[5] This frequency is somewhat arbitrarily defined as it does not have to be equal to ν_{eff} above, but is a matter of definition. The choice of ν_c for *Planck* detectors and frequency channels is discussed further in Sect. 3.2.1.

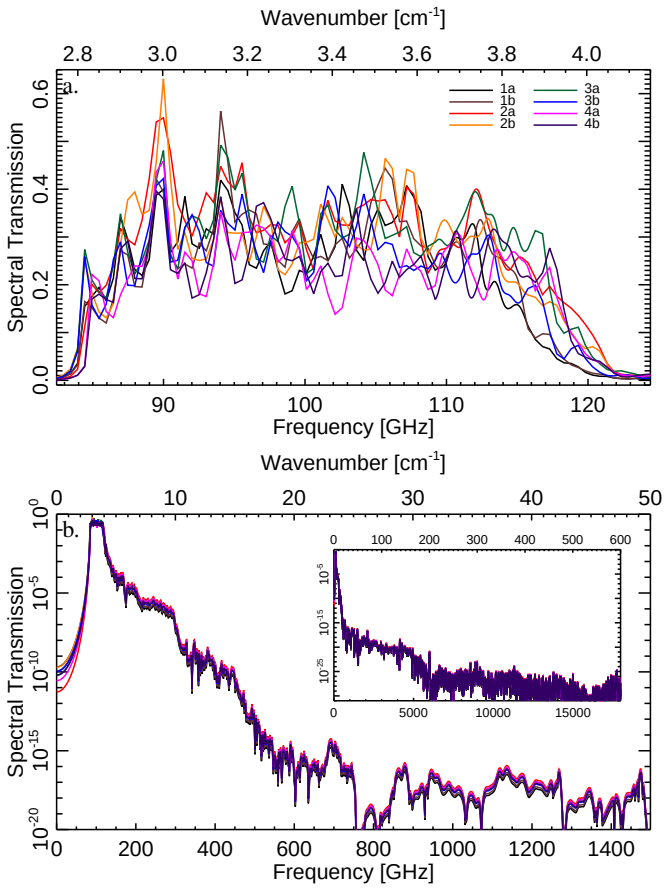

Fig. 5. The detector spectral transmission profiles for the HFI 100 GHz detectors.

3. Results

This section presents data products derived from the HFI detector spectral responses described above. This includes band-average spectra, along with unit conversion and colour correction algorithms and coefficients.

3.1. Frequency Channel-Average Spectra

Frequency channel-average transmission spectra, i.e., band-average spectra, are derived to complement the HFI frequency channel maps of various components (Planck Collaboration XII 2013). To produce band-average spectra, individual detector spectra of a given frequency channel are weighted by a detector scaling factor to mimic the proportional weighting applied in the HFI mapmaking algorithms (Planck Collaboration VI (2013) and Planck Collaboration VIII (2013)). This scaling factor, i.e., w_i, is based on relative noise levels, spectral response, and instrument scan strategy, all of which are described below. Although efforts were made to duplicate the mapmaking routines, the determination of the band-average transmission spectra is similar, but not identical, to its mapmaking counterpart. The method used to determine the band-average transmission spectra is described below. The individual detector weights described in Sect. 3.1.1 are identical to those used in the mapmaking scripts. The divergence lies in the hit-map normalization (Eq. 6), and the CMB normalization (Sect. 3.1.3). The hit map normalization could fully reproduce the approach of the mapmaking routines if an average were produced for each map-pixel (see Sect. 3.4), rather than producing a single scalar w_i coefficient for each de-

Table 2. HFI spectral response diagnostic parameters

Spectrum	ν_{on} [GHz]	ν_{off} [GHz]	$\Delta\nu$ [GHz]	ν_{cen} [GHz]	ν_{eff} [GHz]	ε_{Int}
100-avg	84.4 ± 0.3	117.36 ± 0.05	32.9 ± 0.3	100.89 ± 0.14	101.31 ± 0.05	0.304 ± 0.003
100-detset1	84.77 ± 0.09	117.81 ± 0.05	33.03 ± 0.11	101.29 ± 0.05	101.43 ± 0.07	0.265 ± 0.002
100-detset2	84.29 ± 0.18	117.14 ± 0.05	32.85 ± 0.19	100.72 ± 0.09	101.25 ± 0.06	0.321 ± 0.003
143-avg	119.994 ± 0.018	165.76 ± 0.04	45.76 ± 0.05	142.875 ± 0.020	142.709 ± 0.015	0.3669 ± 0.0006
143-detset1	120.05 ± 0.03	160.18 ± 0.09	40.13 ± 0.10	140.12 ± 0.05	141.45 ± 0.03	0.4614 ± 0.0017
143-detset2	118.95 ± 0.08	164.9 ± 0.8	45.9 ± 0.8	141.9 ± 0.4	142.27 ± 0.02	0.379 ± 0.007
143-SWBs	120.17 ± 0.03	166.308 ± 0.018	46.14 ± 0.04	143.238 ± 0.018	143.96 ± 0.03	0.3123 ± 0.0007
217-avg	188.892 ± 0.011	253.419 ± 0.007	64.527 ± 0.013	221.156 ± 0.006	221.914 ± 0.005	0.33850 ± 0.00012
217-detset1	183.3 ± 0.3	253.606 ± 0.020	70.3 ± 0.3	218.46 ± 0.13	220.548 ± 0.009	0.3053 ± 0.0011
217-detset2	182.159 ± 0.013	253.592 ± 0.007	71.433 ± 0.016	217.875 ± 0.007	220.614 ± 0.009	0.34838 ± 0.00018
217-SWBs	189.02 ± 0.03	253.247 ± 0.013	64.22 ± 0.04	221.136 ± 0.017	222.957 ± 0.008	0.3226 ± 0.0002
353-avg	306.8 ± 0.6	408.22 ± 0.02	101.4 ± 0.6	357.5 ± 0.3	361.289 ± 0.008	0.335 ± 0.002
353-detset1	303.582 ± 0.015	406.333 ± 0.017	102.75 ± 0.02	354.957 ± 0.011	359.156 ± 0.011	0.29902 ± 0.00014
353-detset2	318.885 ± 0.014	407.86 ± 0.02	88.97 ± 0.03	363.372 ± 0.013	360.870 ± 0.012	0.28730 ± 0.00015
353-SWBs	306.3 ± 0.4	408.81 ± 0.03	102.5 ± 0.4	357.56 ± 0.18	361.921 ± 0.011	0.3575 ± 0.0013
545-avg	469.5 ± 0.5	640.81 ± 0.03	171.3 ± 0.5	555.2 ± 0.3	557.54 ± 0.03	0.2612 ± 0.0008
545-detset1	466.44 ± 0.02	642.36 ± 0.04	175.91 ± 0.04	554.40 ± 0.02	557.86 ± 0.03	0.28031 ± 0.00013
545-detset2	470.9 ± 0.3	638.52 ± 0.11	167.6 ± 0.4	554.73 ± 0.17	556.85 ± 0.05	0.2143 ± 0.0005
857-avg	743.9 ± 0.4	989.78 ± 0.08	245.9 ± 0.4	866.8 ± 0.2	862.68 ± 0.05	0.2165 ± 0.0004
857-detset1	736.9 ± 0.7	990.38 ± 0.06	253.4 ± 0.7	863.7 ± 0.4	863.42 ± 0.06	0.2121 ± 0.0006
857-detset2	741.79 ± 0.13	987.01 ± 0.10	245.22 ± 0.17	864.40 ± 0.08	861.74 ± 0.07	0.21419 ± 0.00017

Table 3. HFI spectral response effective frequencies

Spectrum	$\nu_{\alpha=-1}$ [GHz]	$\nu_{\alpha=2}$ [GHz]	$\nu_{\alpha=4}$ [GHz]
100-avg	100.36 ± 0.05	103.24 ± 0.05	105.25 ± 0.04
100-detset1	100.49 ± 0.07	103.35 ± 0.06	105.34 ± 0.06
100-detset2	100.31 ± 0.07	103.19 ± 0.06	105.21 ± 0.05
143-avg	141.362 ± 0.015	145.457 ± 0.014	148.234 ± 0.013
143-detset1	140.11 ± 0.03	144.22 ± 0.02	147.05 ± 0.02
143-detset2	140.91 ± 0.02	145.05 ± 0.02	147.90 ± 0.02
143-SWBs	142.64 ± 0.03	146.63 ± 0.02	149.28 ± 0.02
217-avg	220.111 ± 0.005	225.517 ± 0.006	229.096 ± 0.007
217-detset1	218.666 ± 0.009	224.312 ± 0.009	228.038 ± 0.010
217-detset2	218.697 ± 0.009	224.429 ± 0.009	228.200 ± 0.010
217-SWBs	221.241 ± 0.008	226.395 ± 0.008	229.834 ± 0.010
353-avg	358.563 ± 0.008	366.763 ± 0.009	372.192 ± 0.010
353-detset1	356.386 ± 0.011	364.744 ± 0.012	370.302 ± 0.013
353-detset2	358.409 ± 0.012	365.850 ± 0.012	370.837 ± 0.013
353-SWBs	359.158 ± 0.011	367.455 ± 0.012	372.930 ± 0.014
545-avg	552.22 ± 0.05	567.596 ± 0.017	576.778 ± 0.014
545-detset1	552.43 ± 0.06	568.12 ± 0.02	577.458 ± 0.017
545-detset2	551.76 ± 0.08	566.48 ± 0.03	575.32 ± 0.02
857-avg	854.69 ± 0.11	877.724 ± 0.018	891.462 ± 0.016
857-detset1	855.33 ± 0.16	878.67 ± 0.02	892.59 ± 0.02
857-detset2	853.89 ± 0.17	876.53 ± 0.03	890.03 ± 0.02

tector. The CMB normalization described here is analogous to the dipole calibration done in the standard HFI mapmaking (but, again, not identical).

3.1.1. Noise Weighting

The HFI detector noise equivalent temperature (NET) estimates (Planck Collaboration VI 2013 and Planck Collaboration VIII 2013) are used to weight the individual detector signal in averaging within data processing. An attempt at duplicating this behaviour is made to obtain multi-detector average spectra. To determine the relative weights of individual detectors within an average, the inverse square of the detector NETs is normalized such that the sum total within the desired detector grouping is unity as follows

$$w_i = \frac{1/(\mathrm{NET})^2}{W} \quad \text{where } W = \sum_i (1/(\mathrm{NET})^2) \quad . \tag{5}$$

The detector NETs and the w_i factors can be found in Planck Collaboration ES (2013). Two detectors have been omitted from contributing towards the band-average spectra due to random telegraphic signal (RTS), i.e., popcorn noise: 143 GHz-8 and 545 GHz-3. The w_i factors introduced here represent a general weighting concept that will be expanded upon further. As a result of this, factors strictly following Eq. 5 will be referred to as $w_{\mathrm{NET}\ i}$ in subsequent sections.

3.1.2. Detector Channel-Map Contribution Weighting

Furthermore, the NET can be scan-normalized using the individual-detector pixel-hit maps available as standard data products (these will be made publicly available in the final release of *Planck* data if not earlier, further details on the hit-maps can be found in Planck Collaboration ES (2013)), i.e.,

$$w_{m,i} = \frac{(\sum_{\theta,\phi} H_{m,i}(\theta,\phi))/(\mathrm{NET}_i)^2}{W} \quad , \tag{6}$$

where W is a normalization term as described above, $H_i(\theta,\phi)$ represents the hit-map counts for a given detector, sky position,

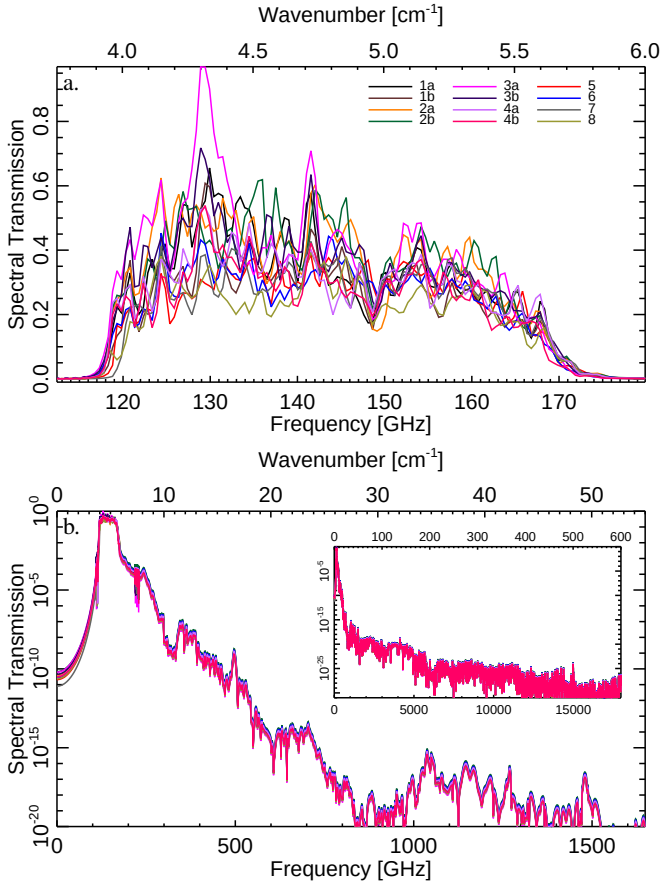

Fig. 6. The detector spectral transmission profiles for the HFI 143 GHz detectors.

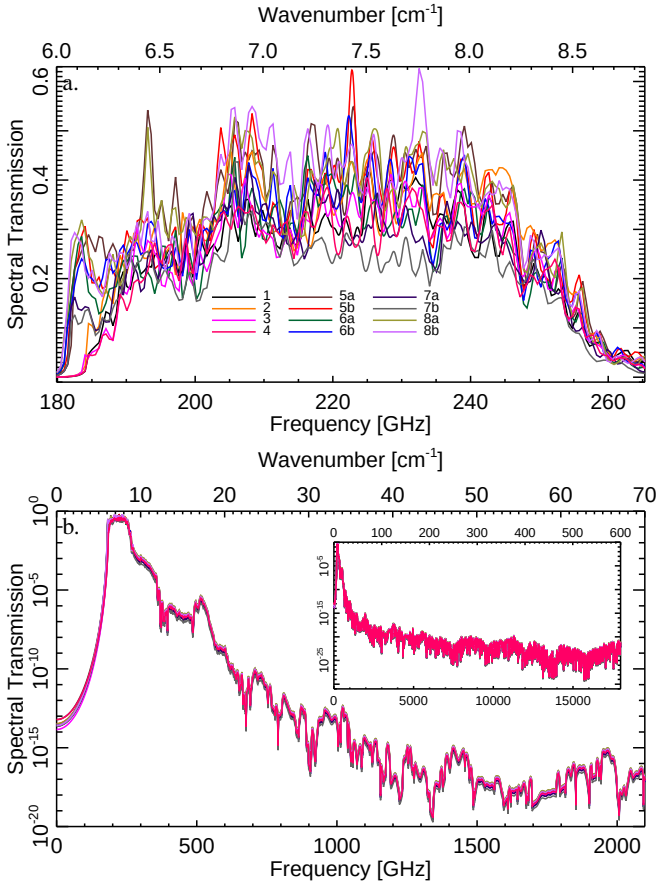

Fig. 7. The detector spectral transmission profiles for the HFI 217 GHz detectors.

and a given map, m (e.g., full-survey, nominal-survey, survey 1, etc.), the $\sum_{\theta,\phi}$ term represents summing over the entire map. A similar approach could be taken where the $\sum_{\theta,\phi}$ summation is omitted; instead of a single w_i factor for a given map, m, this would result in a map of weighting factors of the same spatial resolution as the map, i.e., $w_i(\theta,\phi)$. An example of this, using the nominal survey and survey 1 results for the 857 GHz band, is shown in Fig. 11 [6] , where it is clear that the 857-4 detector contributes less to the maps.

A global factor, $w_{\mathrm{H\,NET}\ i}$, can be obtained from each $w_i(\theta,\phi)$ map by choosing the statistical mean, or median, of the map, by taking the peak of a histogram of the map values, or through choosing some other diagnostic method. Fig. 12 illustrates histograms based on the detector $w_{m,i}(\theta,\phi)$ maps for the HFI full survey, nominal survey, and, in the 100 GHz case, survey 1. Similar histograms were also computed for individual sky surveys (HFI completed 5 fully sky surveys), masked surveys (masking varying percentages of the galactic plane and bright sources), and detector sub-set maps (see Table 4); these have been omitted from Fig. 12 for clarity. For each HFI detector included in the plot, the dashed-dotted vertical lines (marked as NET) indicate the $w_{\mathrm{NET}\ i}$ factors resultant from Eq. 5, while the long-dashed vertical bars (marked as H NET) indicate those resultant from Eq. 6; these coefficients are generated from the full survey $w_{m,i}(\theta,\phi)$ map histograms. Similar results are available for various subsets, all converging towards the full survey values (more detailed figures for each of the HFI bands, and various data sub-sets, are found in Planck Collaboration ES (2013)). The full survey values are displayed as they present stronger convergence than any given subset of the data. The incorporation of the detector hit count into the band-average scaling factors ensures that the resultant frequency channel spectra best represents the effective transmission spectrum for a given map. This is demonstrated by the difference in position of the NET and H NET markings on the figure. In other words, the *Planck* scanning strategy is an important consideration in determining the band-average spectra due to relative hit-counts and integration time changing for different detectors and sky positions.

The 857 GHz example shown is a special case, as the 857-4 bolometer exhibits higher noise properties than it's counterparts. The 857-4 detector contribution relative weight is thus much less than the other 857 GHz detectors. The 857-4 histogram (Fig. 12.b) is not symmetric, with an inflated tail towards zero weight. As a result, the 857 $w_{m.i}$ scalar value is intentionally off-peak by a small factor.

The band-average spectra made available for distribution are thus based on the $w_{m,i}$ values from the full survey maps. While the nominal band-average spectra are produced using the detector-weight histogram peak values, the effects of using off-peak histogram weights on the resultant band-average spectra were investigated. Using compatible weight factors ($\sum = 1$) from the histogram tails produce band-average spectra that vary from the nominal band-average spectra at the percent level.

[6] This figure, and subsequent map figures within this paper, were produced using a modified version of the HEALPix software routines (Górski et al. 2005).

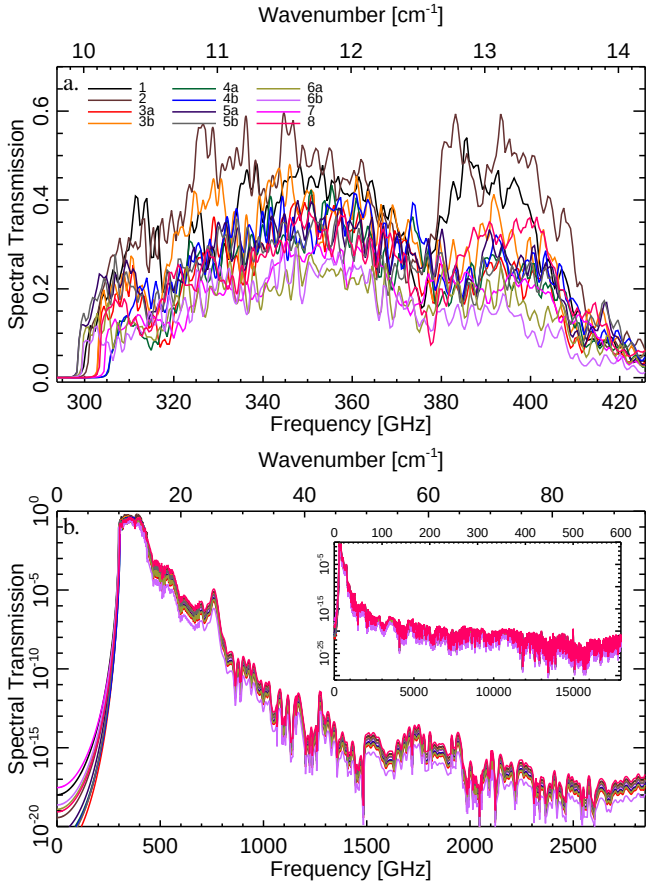

Fig. 8. The detector spectral transmission profiles for the HFI 353 GHz detectors.

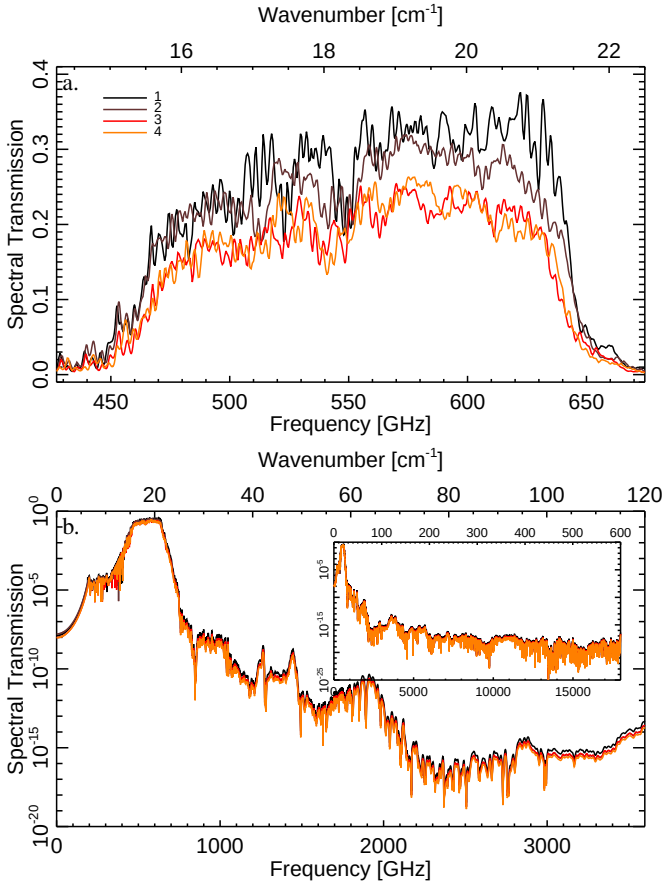

Fig. 9. The detector spectral transmission profiles for the HFI 545 GHz detectors.

3.1.3. Photometric Bandpass Averaging

A map from detector i, m_i, is given by

$$m_i = K_i \frac{1+\eta_i}{2} \epsilon_i \int d\nu (A\Omega)_\nu \tau_i(\nu) dI_\nu \quad [\mathrm{K_{CMB}}], \tag{7}$$

where K_i is the photometric dipole calibration factor (e.g., $\mathrm{K_{CMB}\,W^{-1}}$), the $(1+\eta_i)/2$ fraction is used to distinguish between spider-web bolometers (SWB)s and polarization sensitive bolometers (PSB)s, $(A\Omega)_\nu$ represents the telescope throughput, $\tau_i(\nu)$ represents the normalized spectral transmission, ϵ_i represents the optical efficiency, and dI_ν represents the differential source intensity (see Eq. 9). As $\tau(\nu)$ is throughput normalized, by virtue of the ratio of the HFI detector spectra against a reference bolometer spectrum within an integrating sphere (see Pajot et al. (2010)), the $(A\Omega)_\nu \tau(\nu)$ term is further reduced to $(A\Omega)_{\nu_c} \tau(\nu)$, i.e., the product of the throughput at the nominal reference frequency and the throughput normalized transmission spectra. For SWBs, the $(1+\eta_i)/2$ coefficient is 1, and for PSBs it is 1/2.

The temperature derivative of the Planck function, evaluated at the CMB temperature, i.e., the CMB dipole, is the principle calibration source for HFI. This is used for the 100 – 353 GHz channels, while FIRAS data, accompanied by a planet-based renormalization, is the calibrator used for the 545 and 857 GHz channels (Planck Collaboration VI 2013). Based on the well known Planck function, $B_\nu(T,\nu)$, the CMB dipole signal is assumed to have the following form:

$$\begin{aligned} b'_\nu &= \left.\frac{\partial B_\nu(T,\nu)}{\partial T}\right|_{T=2.7255\ \mathrm{K}} \\ &= \left[\frac{2h\nu^3}{c^2(\exp[h\nu/(KT)]-1)}\right]\left(\frac{\exp[h\nu/(KT)]}{\exp[h\nu/(KT)]-1}\right) \\ &\times \left(\frac{h\nu}{KT^2}\right)\Bigg|_{T=2.7255\ \mathrm{K}} \quad \left[\frac{\mathrm{W}}{\mathrm{m^2\,sr\,Hz\,K}}\right] \quad , \end{aligned} \tag{8}$$

and the differential source intensity is thus given by

$$dI_\nu = b'_\nu dT_{\mathrm{CMB}} \quad \left[\frac{\mathrm{W}}{\mathrm{m^2\,sr\,Hz}}\right] \quad . \tag{9}$$

All of the terms outside of the integral in Eq. 7 can be replaced by a single constant, A_i, as follows

$$A_i = K_i \frac{1+\eta_i}{2} (A\Omega)_{\nu_c} \epsilon_i \quad \left[\frac{\mathrm{K_{CMB}\,m^2\,sr}}{\mathrm{W}}\right]. \tag{10}$$

If the source dI_ν is a dipole CMB spectrum, then the map itself should be given by $m_i = dT_{\mathrm{CMB}}$, therefore

$$A_i = \left(\int d\nu \tau^i(\nu) b'_\nu\right)^{-1} = K_i \frac{1+\eta_i}{2} (A\Omega)_{\nu_c} \epsilon_i \quad \left[\frac{\mathrm{K_{CMB}\,m^2\,sr}}{\mathrm{W}}\right]. \tag{11}$$

The corresponding channel map, M, is given as a weighted combination of the detectors comprising that channel. For individual

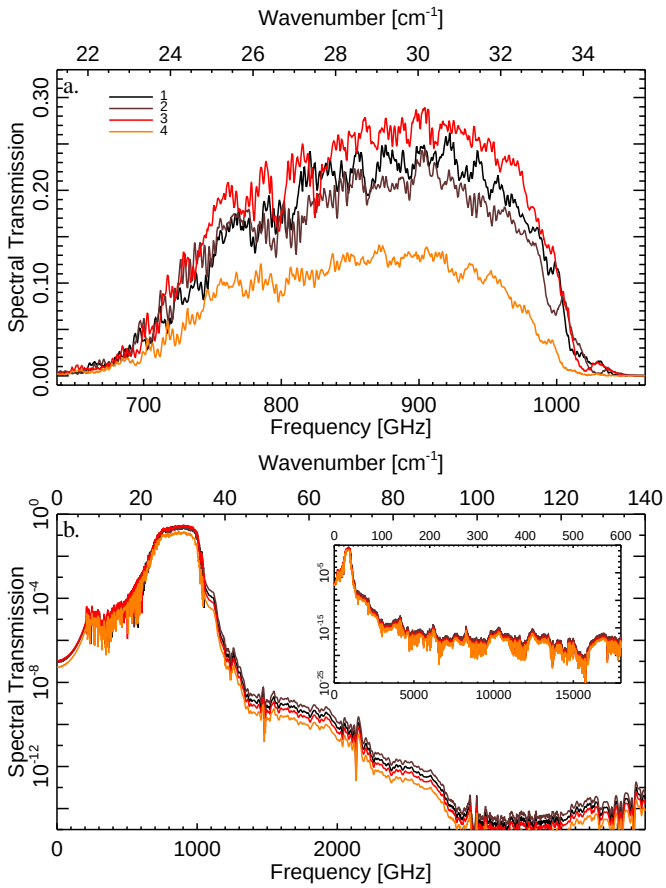

Fig. 10. The detector spectral transmission profiles for the HFI 857 GHz detectors.

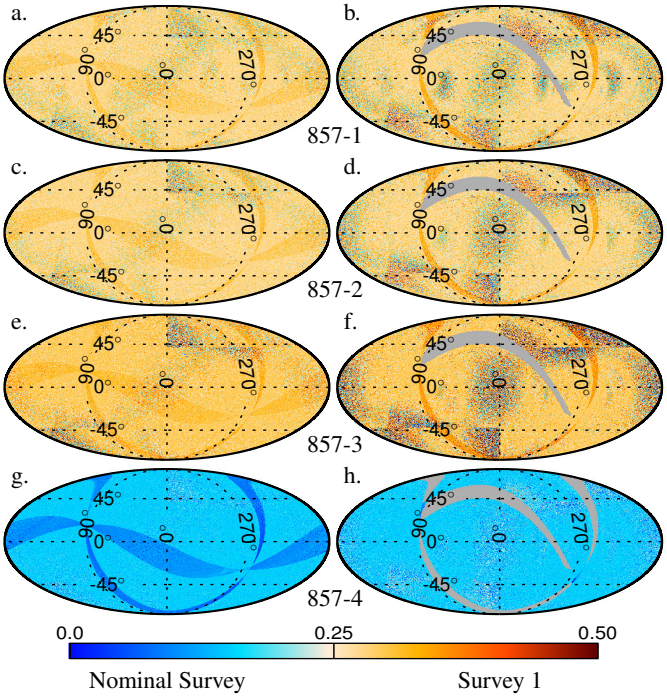

Fig. 11. Detector relative map contribution weight factors, i.e., $w_{m,i}$ as above, for the 857 GHz detectors. The left half represent the nominal survey (a., c., e., g.), while the right half represent the survey 1 subset of the data (b., d., f., h.). Data corresponding to detectors 1 through 4 are grouped in rows, i.e., 857-1 is illustrated in (a.,b.), and 857-2,-3, and -4 are found in (c.,d.), (e.,f.), and (g.,h.), respectively. The grey shaded regions indicate where there was no sky coverage.

weightings of w_i, the map, M, neglecting polarization effects for now, is given by

$$M = \frac{\Sigma_i(w_i m_i)}{\Sigma_i w_i} \quad [\mathrm{K_{CMB}}]. \tag{12}$$

Expanding this expression to include Eqs. 7, 10, and 11, we get

$$\begin{aligned} M &= \left(\frac{1}{\Sigma_i w_i}\right) \sum_i \left(w_i A_i \int d\nu \tau_i(\nu) dI_\nu\right) \\ &= \int d\nu \left(\frac{\Sigma_i(w_i A_i \tau_i(\nu))}{\Sigma_i w_i}\right) dI_\nu \quad [\mathrm{K_{CMB}}] \end{aligned} . \tag{13}$$

It is clear that the transmission and source components of the spectrum are separable, with the effective spectral response given by

$$A\tau(\nu) = \frac{\Sigma_i(w_i A_i \tau_i(\nu))}{\Sigma_i w_i} \quad \left[\frac{\mathrm{K_{CMB}\,m^2\,sr}}{\mathrm{W}}\right], \tag{14}$$

where A is an arbitrary scaling factor such that

$$M = A \int d\nu \tau(\nu) dI_\nu \quad [\mathrm{K_{CMB}}]. \tag{15}$$

Similar to the derivation of Eq. 11, for a CMB dipole source, $M = dT_{\mathrm{CMB}}$ and

$$A = \left(\int d\nu \tau(\nu) b'_\nu\right)^{-1} \quad \left[\frac{\mathrm{K_{CMB}\,m^2\,sr}}{\mathrm{W}}\right]. \tag{16}$$

Equation 14 can be rearranged to solve for $\tau(\nu)$ as follows

$$\begin{aligned} \tau(\nu) &= \left(\frac{1}{A}\right) \left(\frac{1}{\Sigma_i w_i}\right) \left[\sum_i (w_i A_i \tau_i(\nu))\right] \\ &= \left(\int d\nu \tau(\nu) b'_\nu\right) \left(\frac{1}{\Sigma_i w_i}\right) \left[\sum_i \left(\frac{w_i \tau_i(\nu)}{\int d\nu \tau_i(\nu) b'_\nu}\right)\right] \end{aligned} . \tag{17}$$

The above expression, however, contains the desired $\tau(\nu)$ on both sides of the equation. Since the right hand instance of $\tau(\nu)$ is within a frequency integral, and thus will only result in a scaling factor to be applied to the average transmission spectrum, an alternate strategy will be used. The CMB-normalized channel transmission spectrum, $\tau'_{\mathrm{CMB}}(\nu)$, is defined as

$$\tau'_{\mathrm{CMB}}(\nu) = \mathrm{Norm}\left[\left(\frac{1}{\Sigma_i w_i}\right) \sum_i \left(\frac{w_i \tau_i(\nu)}{\int d\nu \tau_i(\nu) b'_\nu}\right)\right] , \tag{18}$$

where Norm$[f(x)]$ is defined as $f(x)/\max[f(x)]$. A CMB-weight factor, $w_{\mathrm{CMB}\ i}$, is introduced to define the contribution of each detector to the bandpass average. The above w_i factors (Eqs. 5 and 6) are coupled with the derivative of the CMB spectral function to determine the noise/CMB-normalized scaling factors as

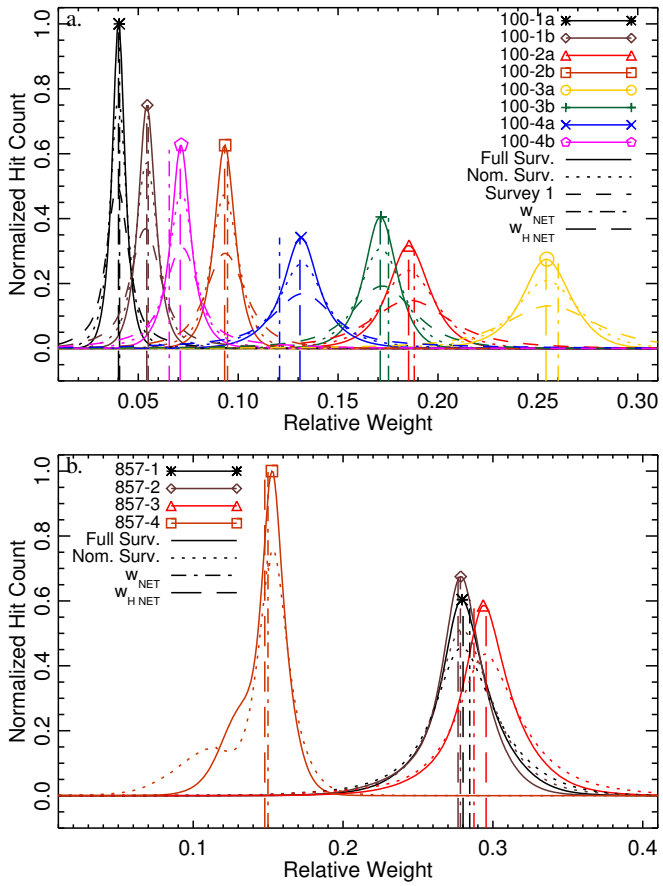

Fig. 12. Histograms of the $w_{m,i}$ band-average spectra scaling factors. Values are shown for 100 GHz (a.) and 857 GHz (b.) detectors, including the full, nominal, and individual surveys (some are omitted for clarity). The vertical bars represent the resultant weight factor both with and without the *Planck* sky coverage and/or hit-maps taken into consideration.

follows

$$w_{\mathrm{CMB}\ i} = \frac{\left[\dfrac{w_i}{(\Sigma_i w_i)\left(\int d\nu \tau_i(\nu) b'_\nu\right)}\right]}{\max\left\{\sum_i \left[\dfrac{w_i \tau_i(\nu)}{(\Sigma_i w_i)\left(\int d\nu \tau_i(\nu) b'_\nu|_{T_{\mathrm{CMB}}}\right)}\right]\right\}} \quad . \tag{19}$$

In the above expression, w_i is a scalar factor unique for each HFI detector. This not need be the case, however, as this case may be more further generalized by allowing the detector weight factor w_i to vary across the sky as in Eq. 6. This generalization results in a $w_{\mathrm{CMB}\ i}(\theta, \phi)$ photometric weighting factor, i.e., the relative weights varies across the sky, and with relative integration time, etc. Fig. 12 illustrates histograms of the detector weight factors across the sky for the HFI full mission data, and various survey sub-sets of this data. The difference between the static w_i factor and the histogram peak value is demonstrated by the vertical bars in the figure. Thus, the frequency band average transmission spectra are comprised of the individual detector spectra proportionately scaled for both the relative response to the CMB spectrum, and the relative noise level within a given channel. The resultant band-average transmission spectra are shown in Fig. 1 above.

As the 545 and 857 GHz channels are calibrated using FIRAS data, and subsequently renormalized using planet observations (Planck Collaboration VI (2013)), rather than using the CMB dipole directly, it is important to investigate the use of Eq. 19 in deriving the band-average spectra for these channels. A comparison using both the w_i and $w_{\mathrm{CMB}\ i}$ scaling factors for the 545 and 857 GHz channels was thus conducted. While these differences for the 100 – 353 GHz channels are at the level of a few percent, they are at the 0.3 – 0.5 % level for the 545 and 857 GHz channels. Furthermore, the differences do not exceed the respective uncertainty of the corresponding detector spectra. As this normalization removes the dependence of the individual $\tau_i(\nu)$ values on an absolute calibration, i.e., the optical efficiency, this CMB-normalization in the band-average spectra is maintained for all of the HFI bands.

3.2. Unit Conversion and Colour Correction

This section presents the formula used to obtain unit conversion and colour correction coefficients for use with the HFI data, and the method used to derive the uncertainties on these coefficients, and the coefficients.

3.2.1. Unit Conversion and Colour Correction Philosophy

Broad-band detection instruments, including photometric instruments using band-defining filters such as HFI, measure power collected via an instrument collecting area for unresolved/point sources, and power collected within a given throughput for extended sources. Although such an instrument directly measures power absorbed by the detectors, it is convenient to relate this power measurement to either flux density (unresolved/point sources) or specific intensity/brightness (extended sources) such that the combined spectral and throughput integrated signal is equal to the measured power. Thus, observation data expressed in units of brightness, specific intensity, or flux density, are intrinsically associated with an assumed reference frequency and spectral energy distribution (SED) profile.

Spectral calibration of broad-band photometric instruments is performed by observation of a source of known SED. Provided that observed sources have a similar SED (within the spectral band) to that of the calibration source, measurements are calibrated by the ratio of the two observations. The general case is that observed sources have a different SED to that of the calibration source(s). Any instrument observation is then related to a calibration observation by expression of both in terms of an equivalent intensity at a specified reference frequency. The equivalent intensity is defined by knowledge of the source SED for a given observation. A colour correction (Griffin et al. 2013) is used to relate measurements of one SED to those of another. There are two equivalent approaches to astronomical colour correction. One approach is to determine the effective frequency that corresponds to the assumed SED and measured intensity, and determine a different reference frequency, based upon a different SED, for any other SEDs of interest. In converting between SED types, the intensity remains the same, but at a different reference frequency. The other approach is to determine the relative intensity for a given reference frequency, so the reference frequency remains the same for various SEDs, but the intensity will vary.

The *Planck* HFI uses two calibration schemes (Planck Collaboration VIII 2013), one based on the differential CMB dipole spectrum, and another based upon the more local astrophysical sources. The 100 – 353 GHz channels are calibrated on the CMB dipole, which follows a $\delta B_\nu/\delta T|_{\mathrm{T_{CMB}}}$ SED profile, where data are provided in units of differential CMB temperature, i.e., $\mathrm{K_{CMB}}$. The 545 and 857 GHz channels are calibrated on a combination of galactic emission (typically dust following an approx. ν^4 SED profile) and planetary emission (of an approx. ν^2 SED profile), where data are provided in units of brightness/intensity, i.e. MJy sr^{-1}. Furthermore, the 545 and 857 GHz data are scaled to equate with an SED following the IRAS convention (Beichman et al. 1988), which has a SED profile of the form νI_ν = constant. It is thus important to express observation data in both formats for various aspects of data analysis. This involves both unit conversion, where data are presented in a different unit, but remain consistent with a given SED (e.g., MJy sr^{-1} can be expressed as an equivalent brightness in K), and colour correction, where data are expressed with respect to a different assumed SED at the same reference frequency (e.g., changing from $\mathrm{K_{CMB}}$ to MJy sr^{-1} with a SED of spectral index −1).

In the millimetre - sub millimetre region of the electromagnetic spectrum, the diffuse emission is made of several components whose summation represents the observed signal. Component separation algorithms (Planck Collaboration XII 2013), when separating physical components with different SED profiles (e.g., emission from the CMB, thermal dust, spinning dust, free-free sources, synchrotron sources, CO lines, etc.), use models or templates for these components. The component separation then must resolve an inverse problem going from several maps of broad-band measurements at different frequencies to component maps. The model is adjusted to minimize residuals through fitting the sum of the components to the measured intensity. It is therefore impractical to have the various components all expressed at different effective frequencies. Thus, *Planck* adopts a fixed reference frequency unit conversion/colour correction where the intensity is corrected for the assumed (or measured) SED of the source or component.

Using $\mathrm{K_{CMB}}$ calibration for the submillimeter channels, especially 857 GHz, should be avoided. This is because the submillimetre IRAS to CMB unit conversion depends heavily on the low-frequency region of the bandpass spectrum (see Fig. 14), which is known with less confidence than the main band. Therefore, the conversion of the 100 – 353 GHz data from a CMB to IRAS SED is less error-prone.

Details on the derivation of the *Planck* unit conversion and colour correction coefficients are provided in the following section.

3.2.2. Coefficient Formula Derivation

The following conversion factors are derived for the individual HFI detectors and the frequency-channel average spectra:

1. Convert [MJy/sr] (IRAS) ⇌ [$\mathrm{K_{CMB}}$].
2. Convert [MJy/sr] (IRAS) ⇌ [$\mathrm{K_{RJ}}$].
3. Convert [$\mathrm{y_{SZ}}$] ⇌ [$\mathrm{K_{CMB}}$].
4. Colour correction (power-law spectra and modified blackbody spectra).
5. CO correction.

In general, the unit conversion terms are arrived at by equating changes in intensity, expressed in various forms. Starting with the general expression $dI_\nu = dI_\nu$; e.g.,

$$dI_\nu = (dI_\nu/dX_i)(dX_i) = (dI_\nu/dX_j)(dX_j) \quad . \tag{20}$$

Each side may also be multiplied by the spectral transmission, $\tau(\nu)$, and integrated across the frequency band as follows

$$\int d\nu\, \tau(\nu) \left(\frac{dI_\nu}{dX_i}\right) dX_i = \int d\nu\, \tau(\nu) \left(\frac{dI_\nu}{dX_j}\right) dX_j \quad . \tag{21}$$

This can be simplified to the form of a unit conversion coefficient

$$\frac{dX_i}{dX_j} = \frac{\int d\nu\, \tau(\nu) \left(\frac{dI_\nu}{dX_j}\right)}{\int d\nu\, \tau(\nu) \left(\frac{dI_\nu}{dX_i}\right)} \quad . \tag{22}$$

In converting to/from $\mathrm{K_{CMB}}$, the derivative of the Planck function at the CMB monopole temperature ($T_{\mathrm{CMB}} = 2.7255$ K, see Fixsen (2009)) will be used (see Eq. 8 and 9).

Conversion to MJy/sr (IRAS) is accomplished using the IRAS convention (Beichman et al. 1988) [7] , $\nu\, dI_\nu$ = constant, such that

$$dI_{\nu\,\mathrm{IRAS}} \equiv \left(\frac{\nu_c}{\nu}\right) dI_c \quad \left[\frac{\mathrm{W}}{\mathrm{m^2\,sr\,Hz}}\right] \quad , \tag{23}$$

where ν_{c} is the band centre frequency and dI_c is the effective intensity at the central frequency for a source of spectral index minus one.

As Rayleigh-Jeans brightness temperature units are often more convenient (i.e., human friendly) than that of W m^{-2} sr^{-1} Hz^{-1} or even MJy sr^{-1}, a flux density to brightness temperature unit conversion is provided using the following relation (Rybicki & Lightman 1986):

$$dT_b = \frac{c^2}{2\nu^2 k} dI_\nu \quad [\mathrm{K_b}] \quad , \tag{24}$$

where $\mathrm{K_b}$ is the temperature expression of flux density, i.e., brightness temperature does not imply a Rayleigh-Jeans spectral profile. The brightness temperature unit of $\mathrm{K_b}$ is selected over $\mathrm{K_{RJ}}$ to avoid any confusion between this definition, and that of a source exhibiting a Rayleigh-Jeans SED profile.

For SZ conversion the following intensity expression, based on the Kompaneets non-relativistic SZ formula (Kompaneets (1957), Sunyaev & Zeldovich (1980), and Grainger (2001)), is used

$$dI_{\nu\,\mathrm{SZ}} = (b'_\nu)\,(T) \left[\left(\frac{h\nu}{kT}\right) \frac{\exp\left[h\nu/(kT)\right] + 1}{\exp\left[h\nu/(kT)\right] - 1} - 4\right] (y_{\mathrm{SZ}})\Big|_{T_{\mathrm{CMB}}} \quad , \quad \left[\frac{\mathrm{W}}{\mathrm{m^2\,sr\,Hz}}\right] \tag{25}$$

where, again, b'_ν is the temperature derivative of the Planck function.

In power-law colour correction, it is assumed that the source intensity follows a power law over the spectral region of interest, i.e., $dI_\nu \propto \nu^\alpha$, providing the following expression

$$dI_{\nu\,\alpha} = \left(\frac{\nu}{\nu_{\mathrm{c}}}\right)^\alpha dI_{\mathrm{c}\,\alpha} \quad \left[\frac{\mathrm{W}}{\mathrm{m^2\,sr\,Hz}}\right] \quad . \tag{26}$$

[7] http://lambda.gsfc.nasa.gov/product/iras/docs/exp.sup/ch6/C3.html

A colour correction to a modified-blackbody of the form $dI_\nu \propto \nu^\beta B_\nu(\nu, T)$ (B_ν defined above) is given by

$$dI_{\nu\,\beta} = \left[\frac{\nu^\beta\, B_\nu(\nu,T)}{\nu_c^\beta\, B_\nu(\nu_c,T)}\right] dI_{c\,\beta} \quad \left[\frac{\mathrm{W}}{\mathrm{m^2\,sr\,Hz}}\right] \quad . \tag{27}$$

For molecular rotational transitions, such as the CO J1-0, ..., J9-8 transitions, the desired specific intensity term is an effective brightness temperature, ΔT_{CO}, in units of K km s^{-1}. For a Doppler line profile, ν is equal to $\nu_{CO}(1+v/c)^{-1}$, which is closely approximated by $\nu_{CO}(1 - v/c)$ for $v << c$. The intensity can be said to be distributed across a narrow velocity distribution, dv [8] , such that the integral over all velocities yields the temperature-velocity effective brightness. To relate the effective brightness across a narrow frequency range, $d\nu$, to frequency units rather than those of velocity, the relationship $d\nu/dv = -\nu_{CO}/c$ is used, i.e.,

$$\Delta T_{CO}|_\nu = \frac{\Delta T_{CO}\left(\frac{\nu_{CO}}{c}\right)}{d\nu} \quad [\mathrm{K}] \quad . \tag{28}$$

It is important to note that the effective brightness temperature, i.e., ΔT_{CO}, is given in units of K km s^{-1} while this brightness distributed across a defined velocity interval (dv), or a defined frequency range ($d\nu$), i.e., $\Delta T_{CO}|_\nu$, is given in units of K. The CO transition intensity is thus given by the following relation

$$\begin{aligned} dI_{CO} &= (\Delta T_{CO}|_\nu)\, b'_{RJ} \\ &= (\Delta T_{CO})\left(\frac{\nu_{CO}}{c\,d\nu}\right) b'_{RJ} \quad \left[\frac{\mathrm{W}}{\mathrm{m^2\,sr\,Hz}}\right] \quad . \end{aligned} \tag{29}$$

The Rayleigh-Jeans(R-J) approximation temperature derivative used above is given as follows

$$\begin{aligned} b'_{RJ} &= \left.\frac{\partial B_{\nu\,RJ}(T,\nu)}{\partial T}\right|_{RJ} \\ &= \frac{2\nu^2 k}{c^2} \quad \left[\frac{\mathrm{W}}{\mathrm{m^2\,sr\,Hz\,K_{RJ}}}\right] \quad . \end{aligned} \tag{30}$$

As the CO transitions occur at discrete frequencies, with line widths much narrower than the spectral resolution of the detector spectral transmission profiles, the CO intensity integral can be approximated by a delta function at the CO frequency, i.e.,

$$\int d\nu \tau(\nu) dI_{CO} \cong \tau(\nu_{CO})\,(\Delta T_{CO})\left(\frac{\nu_{CO}}{c}\right) b'_{RJ}|_{\nu_{CO}} \quad \left[\frac{\mathrm{W}}{\mathrm{m^2\,sr}}\right] \quad . \tag{31}$$

The *Planck* spectral response conversion coefficients are therefore given by the following ratios

$$U_{\mathrm{KCMB\_to\_MJy/sr}} = \frac{\int d\nu\, \tau(\nu) b'_\nu}{\int d\nu\, \tau(\nu)(\nu_c/\nu)} \times 10^{20} \quad \left[\frac{\mathrm{MJy/sr}}{\mathrm{K_{CMB}}}\right] \tag{32}$$

$$U_{\mathrm{KCMB\_to\_ySZ}} = \frac{\int d\nu\, \tau(\nu) b'_\nu}{\int d\nu \left\{ \tau(\nu)\,(b'_\nu)\,(T)\left[\left(\frac{h\nu}{kT}\right)\frac{\exp[h\nu/(kT)]+1}{\exp[h\nu/(kT)]-1} - 4\right]\Big|_{T_{CMB}}\right\}} \quad , \quad \left[\frac{1}{\mathrm{K_{CMB}}}\right] \tag{33}$$

$$U_{\mathrm{SI\text{-}1\_to\_}\alpha} = \frac{\int d\nu\, \tau(\nu)(\nu_c/\nu)}{\int d\nu\, \tau(\nu)(\nu/\nu_c)^\alpha} \quad \left[\frac{\mathrm{Hz}}{\mathrm{Hz}}\right] \quad , \tag{34}$$

$$U_{\mathrm{SI\text{-}1\_to\_}\beta} = \frac{\int d\nu\, \tau(\nu)(\nu_c/\nu)}{\int d\nu\, \tau(\nu)(\nu/\nu_c)^\beta \left[\frac{\nu^\beta\, B_\nu(\nu,T)}{\nu_c^\beta\, B_\nu(\nu_c,T)}\right]} \quad \left[\frac{\mathrm{Hz}}{\mathrm{Hz}}\right] \quad , \tag{35}$$

and

$$U_{CO} = \frac{\tau(\nu_{CO})\left(\frac{\nu_{CO}}{c}\right) b'_{RJ}|_{\nu_{CO}}}{\int d\nu\, \tau(\nu) b'_\nu} \quad \left[\frac{\mathrm{K_{CMB}}}{\mathrm{K_{RJ}\,km\,s^{-1}}}\right] \quad . \tag{36}$$

3.2.3. HFI Unit Conversion and Colour Correction Coefficients

This section presents unit conversion and colour correction coefficients resultant from the above relations and HFI detector spectra. Similar values for the LFI may be found in Planck Collaboration II (2013, e.g., Table 8). In addition to processing data from individual detectors, HFI data are processed to provide band-average frequency maps, and sub-band average frequency maps. The sub-band frequency maps are comprised of three sets, DetSet1, DetSet2, and SWB (i.e., spiderweb bolometers only). These groupings for the HFI detectors are summarized in Table 4. Results presented here are restricted to the average spectra. Similar data for individual detectors is available in Planck Collaboration ES (2013). Table 5 provides multiplicative unit conversion coefficients to go from MJy sr^{-1} to K_b brightness temperature. [9] Table 6 provides unit conversion coefficients for band-average spectra. An example dust colour correction coefficient is also provided in the table, which has assumed a dust SED with a spectral index of 4. Figure 13 illustrates the variation in a colour correction coefficient as a function of power-law spectral index. Colour correction coefficients for planets within our Solar system (HFI calibration sources) have also been determined; Table 7 provides these coefficients for the band-average spectra; these are needed, e.g., for the HFI beam calibration (Planck Collaboration VII 2013). The CO conversion coefficients are provided in Sect. 4.2.1 and in Planck Collaboration ES (2013).

The multiplicative unit conversion and colour correction coefficients are to be used as follows. Take, for example, a dust region within a *Planck* 100 GHz band-average map with an estimated intensity of 10 K_{CMB}. To convert this intensity to an equivalent specific intensity in MJy sr^{-1} (IRAS), the original intensity should be multiplied by the unit conversion coefficient of 244.1 (see Table 6) to obtain a brightness intensity of 2441 MJy sr^{-1}. If the dust can be approximated to follow a SED spectral profile with a spectral index of 4, then the colour correction would be applied by multiplying the 2441 MJy sr^{-1} by the colour correction coefficient of 0.8938 to convert *from* a spectral index of −1 *to* a spectral index of 4; yielding 2182 MJy sr^{-1}. The fourth column of Table 6 provides the combined unit conversion / colour correction as the product of the second and third columns. If the same 10 K_{CMB} intensity were found within a 100 GHz detset1 map, then the resulting colour-corrected dust

[8] The variable v is used to denote velocity in units of km s^{-1}, while the variable ν is used to denote frequency in units of Hz (or equivalent).

[9] This unit conversion is independent of spectral index, and the brightness temperature does not imply a Rayleigh-Jeans spectral profile.

Table 4. HFI sub-band average groupings

Band [GHz]	DetSet1	DetSet2	SWB
100 GHz	1a/b, 4a/b	2a/b, 3a/b	
143 GHz	1a/b, 3a/b	2a/b, 4a/b	5,6,7
217 GHz	5a/b, 7a/b	6a/b, 8a/b	1,2,3,4
353 GHz	3a/b, 5a/b	4a/b, 6a/b	1,2,6,7
545 GHz	1, 2	4	
857 GHz	1, 2	3, 4	

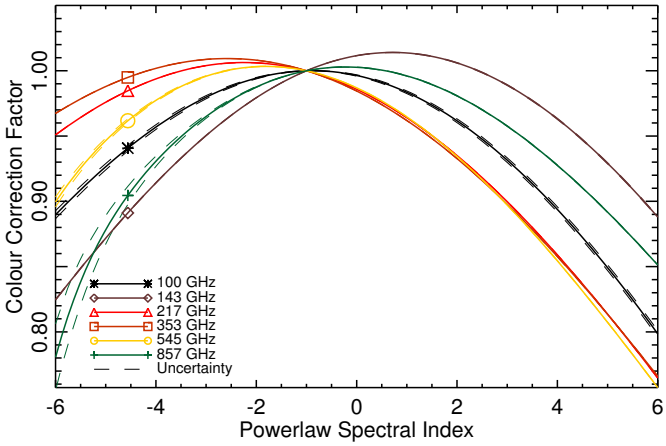

Fig. 13. Colour correction coefficients for varying spectral index for the HFI band-average spectra. Similar data for individual detectors and DetSet subsets are available in Planck Collaboration ES (2013).

Table 5. HFI flux density to brightness temperature unit conversion coefficients

Band [GHz]	U_C [$K_{RJ}MJy^{-1}$ sr]
100	0.0032548074
143	0.0015916707
217	0.00069120334
353	0.00026120163
545	0.00010958025
857	0.000044316316

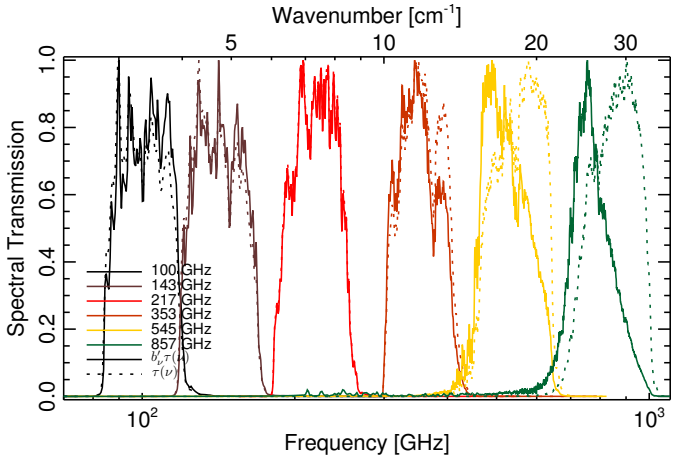

Fig. 14. Product of the the HFI band-average spectra, $\tau(\nu)$, with the CMB dipole spectral profile, i.e., $b'_\nu\tau(\nu)$ (Eq. 8) shown using solid curves. The nominal spectra shown for as dotted curves for reference.

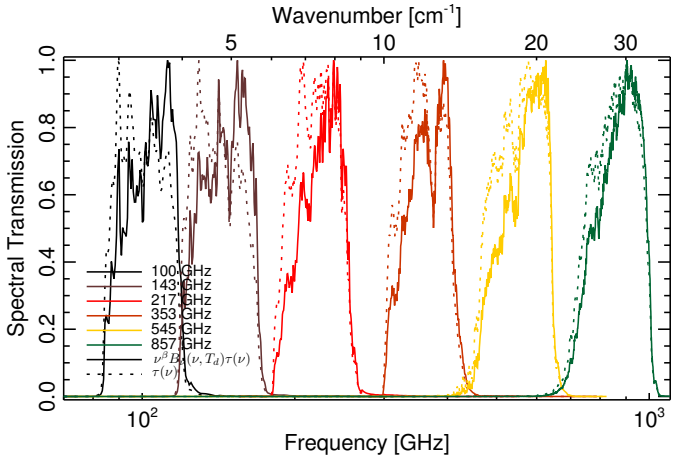

Fig. 15. Product of the band-average spectra with an example dust spectrum (T_d =18 K, β_d =1.5, Eq. 27) shown using solid curves. The nominal spectra are shown as dotted curves for reference.

intensity would be 2176 MJy sr^{-1}. To colour correct *from* a spectral index of 4 *to* a spectral index of −1, one would divide the intensity by the colour correction coefficient found in the third column of Table 6.

To demonstrate the relative contribution of the various regions of the spectral bands on the CMB dipole signal, Fig. 14 illustrates the $b'_\nu\tau(\nu)$ product for the band-average spectra (similar results are found for the individual detector spectra). It is important to note that for the 857 GHz channel, and partly for the 545 GHz channel, the unit conversion integral (Eq. 8 and 32) is dominated by the low-frequency portion of the band. Any residual systematics in the transmission spectra may cause undesired errors, e.g., in the conversion of 857 GHz (or 545 GHz) data to units of K_{CMB}. It is preferred, for example, to convert the lower frequency channel data to MJy sr^{-1} when needed, rather than converting the 857 GHz data into K_{CMB} units. For comparison, Fig. 15 illustrates the product of the band-average spectra with a sample dust spectrum, with a modified blackbody of dust temperature, T_d =18 K and β_d =1.5 (see Eq. 27).

Another investigation was conducted in order to understand the effect of a hypothetical systematic bias in the spectral response data. This study involved scaling the transmission spectra by an scaling term with a linear dependence on frequency, such that it is unity valued on the nominal band centre (i.e., 100, 143, 217, 353, 545, and 857 GHz for the respective bands), is centred on the nominal band centre frequency, and has a linear deviation towards a specified value, $m_{\rm ref}$, at the $\nu_c \pm 15\,\%$ band edges. Fig. 16 illustrates the normalized variation of a combined unit conversion and colour correction for each of the HFI bands, over a range of linear slopes spanning $m_{\rm ref} \in [-2\,\%, 2\,\%]$. The selected example illustrates a conversion from K_{CMB} to MJy sr^{-1} and a colour correction from spectral index of −1 to the dust profile described above. The spectral uniformity of the reference bolometer used in characterizing the HFI detector spectral response (see Planck Collaboration ES (2013)) is estimated to be at

Table 6. HFI unit conversion coefficients

Band [GHz]	$U_{\rm C\ IRAS}$ [MJy/sr/$K_{\rm CMB}$]	$C_{\rm C\ dust}$	$(U_{\rm C\ IRAS})(C_{\rm C\ dust})$ [MJy/sr/$K_{\rm CMB}$]	$U_{\rm C\ SZ}$ [$y_{SZ}/K_{\rm CMB}$]
100-avg	244.1 ± 0.3	0.8938 ± 0.0019	218.2 ± 0.3	-0.24815 ± 0.00007
100-detset1	244.9 ± 0.4	0.889 ± 0.003	217.6 ± 0.4	-0.24833 ± 0.00010
100-detset2	243.8 ± 0.4	0.896 ± 0.003	218.4 ± 0.4	-0.24807 ± 0.00009
143-avg	371.74 ± 0.07	0.9632 ± 0.0004	358.04 ± 0.07	-0.35923 ± 0.00006
143-detset1	365.03 ± 0.15	1.0058 ± 0.0009	367.15 ± 0.15	-0.35398 ± 0.00011
143-detset2	369.30 ± 0.13	0.9773 ± 0.0008	360.93 ± 0.13	-0.35743 ± 0.00010
143-SWBs	378.58 ± 0.14	0.9238 ± 0.0008	349.74 ± 0.14	-0.36446 ± 0.00011
217-avg	483.690 ± 0.012	0.85895 ± 0.00011	415.465 ± 0.012	5.152 ± 0.006
217-detset1	480.36 ± 0.02	0.88411 ± 0.00016	424.69 ± 0.02	7.212 ± 0.019
217-detset2	480.314 ± 0.019	0.88235 ± 0.00017	423.804 ± 0.019	7.046 ± 0.018
217-SWBs	486.331 ± 0.018	0.84069 ± 0.00015	408.855 ± 0.018	4.236 ± 0.006
353-avg	287.450 ± 0.009	0.85769 ± 0.00011	246.543 ± 0.009	0.161098 ± 0.000011
353-detset1	289.620 ± 0.012	0.88255 ± 0.00015	255.606 ± 0.012	0.163757 ± 0.000014
353-detset2	287.967 ± 0.013	0.86548 ± 0.00014	249.229 ± 0.013	0.160904 ± 0.000014
353-SWBs	286.786 ± 0.011	0.84997 ± 0.00014	243.759 ± 0.011	0.160456 ± 0.000013
545-avg	58.04 ± 0.03	0.85444 ± 0.00016	49.59 ± 0.03	0.06918 ± 0.00003
545-detset1	58.02 ± 0.03	0.8513 ± 0.0002	49.39 ± 0.03	0.06924 ± 0.00004
545-detset2	58.06 ± 0.05	0.8612 ± 0.0003	50.00 ± 0.05	0.06905 ± 0.00005
857-avg	2.27 ± 0.03	0.9276 ± 0.0002	2.09 ± 0.03	0.0380 ± 0.0004
857-detset1	2.26 ± 0.03	0.9231 ± 0.0003	2.08 ± 0.03	0.0380 ± 0.0005
857-detset2	2.27 ± 0.04	0.9333 ± 0.0003	2.11 ± 0.04	0.0380 ± 0.0005

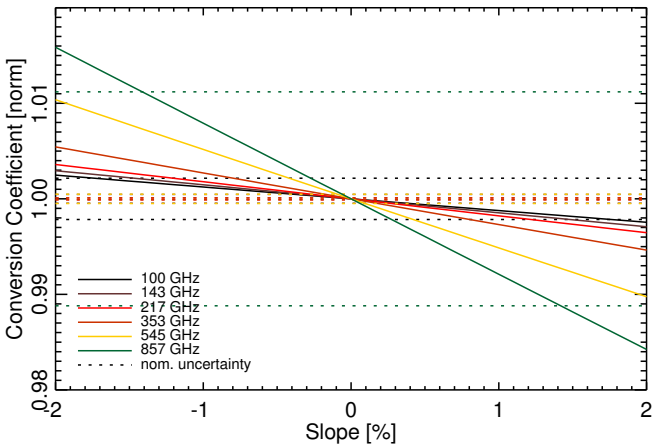

Fig. 16. Variation of combined unit conversion / colour correction with a hypothetical systematic spectral error as described in the text.

the level of 1 %; this is the motivation behind the type of systematic distortion introduced in this study. The figure demonstrates that a systematic reference spectral flatness error, as described above, results in biased unit conversion / colour correction coefficients. The introduced coefficient bias has a magnitude that scales linearly with the slope of the spectral flatness systematic error introduced. The 857 GHz channel fluctuates the most due to the the dominance of the unit conversion on the low-frequency region of the band, and the dominance of the selected colour correction on the high-frequency portion of the band, as illustrated in Figs. 14 and 15.

3.2.4. Unit Conversion and Colour Correction Software Tools

A set of software tool, written in the Interactive Data Language (IDL) has been developed for distribution with the HFI detector spectra and *Planck* data. This tool package, herein the UcCC package, uses the transmission spectra provided in a .fits file format, and computes the unit conversion and colour correction factors using the relations derived above. The UcCC tools may be used to determine colour corrections for a variety of spectral profiles, including powerlaw and modified blackbody as described above as well as user defined source spectra. these tools also provide coefficient uncertainty as an optional output. The UcCC code package may be obtained from the *Planck* Legacy archive, with further details on their use provided in Planck Collaboration ES (2013).

3.3. Error Propagation

The uncertainty of the HFI detector spectral response and band-average spectral response was propagated to the coefficient factors described above. For each of the correction factors shown (Eq. 32 – 36), the measured spectral transmission profile, $\tau(\nu)$, is used along with the associated spectral uncertainty. An additional uncorrelated uncertainty was repeatedly introduced to the spectrum under consideration, where a Gaussian noise distribution in frequency space was weighted by the uncertainty in $\tau(\nu)$, with the resultant spectrum plus noise then used in the calculation of the desired coefficient. The uncertainty values for coefficients shown in this work correspond to the statistical evaluation of 10 000 trials in each instance. These uncertainties reflect only the propagation of the spectral uncertainty into the coefficient and may not represent the full uncertainty in every case. An evaluation of some potential sources of systematic uncertainty is included in Sect. 4 below.

Table 7. HFI planet colour correction coefficients

Band [GHz]	Mars	Jupiter	Saturn	Uranus	Neptune
100-avg	0.9613 ± 0.0017	0.962 ± 0.005	0.963 ± 0.004	0.9692 ± 0.0011	0.9741 ± 0.0010
143-avg	1.0069 ± 0.0009	1.007 ± 0.004	1.008 ± 0.003	1.0122 ± 0.0002	1.0127 ± 0.0002
217-avg	0.9355 ± 0.0002	0.9376 ± 0.0016	0.9529 ± 0.0010	0.94897 ± 0.00004	0.96195 ± 0.00004
353-avg	0.93365 ± 0.00005	0.9385 ± 0.0004	0.94145 ± 0.00014	0.94870 ± 0.00004	0.93676 ± 0.00004
545-avg	0.93603 ± 0.00010	0.92946 ± 0.00009	0.81721 ± 0.00009	0.95148 ± 0.00009	0.96409 ± 0.00009
857-avg	0.98273 ± 0.00014	0.99918 ± 0.00014	0.99923 ± 0.00014	0.99210 ± 0.00013	0.99815 ± 0.00013

3.4. Band-average Coefficient Maps

Using the $W_{m,i}(\theta, \phi)$ maps described above (Eq. 6), band-average spectra may be computed for every pixel of a sky map (rather than integrating the relative weights across the map). Thus, for frequency channel maps, coefficient sky maps may be generated for individual surveys and combinations of surveys. For individual detectors, the response is expected to be constant across the sky, but for channel average data, the sky coverage and relative noise causes variations in the proportional averaging. An example band-average coefficient map is shown in Fig. 17, where the 353 GHz combined K_{CMB} to MJy sr^{-1} (IRAS) unit conversion and IRAS to dust (see Sect. 4.2.2) colour corrections are shown for the nominal and individual surveys.

These coefficient maps can be used to investigate differences between surveys, and the coefficient variation across a region of interest can be compared to the magnitude of other sources of error, providing a probe of the effect of scan strategy, integration time, and relative intra-band detector noise levels on map consistency and unit conversion coefficients. Histograms of the coefficient sky maps provide a verification of the Monte-carlo uncertainty estimates in much the same way that the weight factor histograms verify the band-average scaling factors (see Fig. 12). For coefficient map histogram distributions that are relatively narrow, i.e., of the same width as the Monte-Carlo simulation based uncertainty estimates, data processing and analysis may be simplified by using static conversion coefficients as opposed to coefficient maps. While these maps are not being provided under the current data release, the discussed histograms have been used to validate the use of scalar unit conversion and colour correction coefficients as opposed to the discussed coefficient maps. The maps within Fig. 17 demonstrate the variation of the band-average unit conversion / colour correction coefficient to be small, typically less than 0.1 %. Histograms of these maps are shown below in Fig. 27. This discussion will continue in greater detail within future work as these levels of coefficient fluctuations at the map level are expected to become more important with polarization analysis.

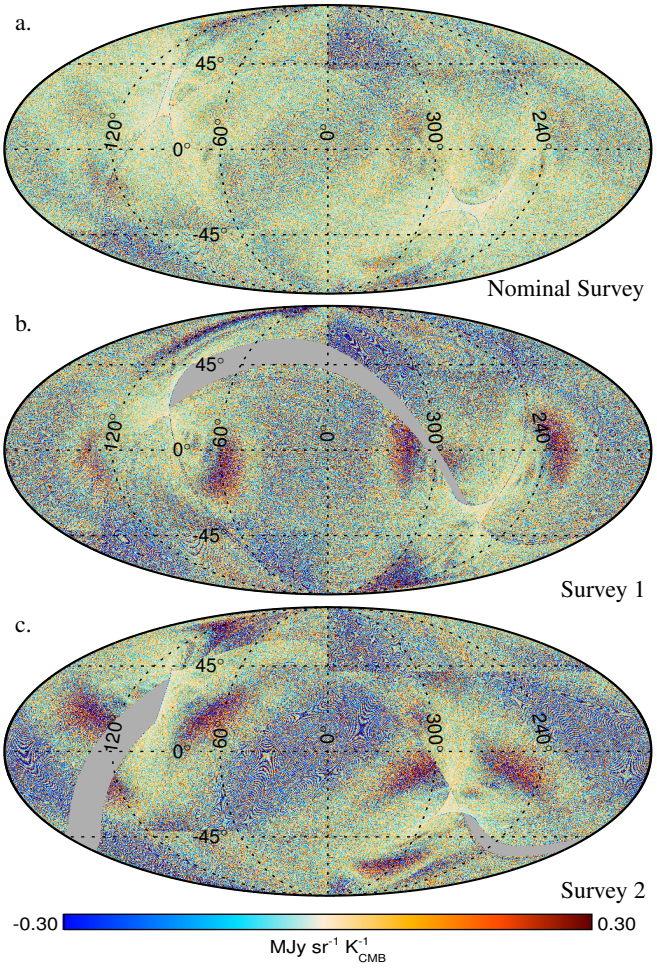

Fig. 17. 353 GHz band-average dust unit conversion and colour correction coefficient maps. The maps show the deviation of the coefficient about the median. The medians in each case are 278.970 (a.), 278.960 (b.), and 278.970 (c.) MJy sr^{-1} K$^{-1}_{CMB}$.

4. Discussion

This section evaluates the HFI detector and band-average spectral response data, and the associated unit conversion and colour correction algorithms and coefficients. This is done through comparison of these data with HFI flight data. HFI detector bandpass mismatch, i.e., the relative difference between an individual detector spectrum and its band-average counterpart, can be compared with variations between individual detector and channel average detector results. Examples include CO, SZ, dust, etc. Out of band signal rejection is verified through comparisons with the HFI Zodiacal light observations, where any out-of-band sky signal received would be evident in the data. As the progress of the HFI polarization data advances, comparisons between spectral response predicted polarization leakage and observed intensity to polarization leakage in HFI maps can also be used to verify the accuracy of the HFI spectral response data.

4.1. Out-of-band Signal Rejection

Each of the HFI bands has a filter stack of 5 low-pass filters with varying cut-off frequencies in order to achieve suitable out-of-band signal rejection. In addition, the 545 and 857 bands also have a high-pass filter dictating the cut-on frequency, which also serves to provide some rejection at much higher frequencies. When the transmission of the individual filters comprising each HFI filter stack was measured, a series of FTS scans were recorded with external low pass filters up to 650 cm^{-1} (approx. 19.5 THz, 15.4 μm). This was not done as a single measurement but a series of experiments to allow the transmission in-band to be measured to higher resolution and S/N. For each of the low pass-filters, the transmission at the high-frequency end dropped to about 10^{-4} to 10^{-6} beyond the cut-off frequency. Given that there are 5 filters in a stack, the out-of-band rejection is very high. The spectral transmission for all frequencies greater than 3 THz is less than 10^{-15} for all HFI bands, reaching as low as 10^{-25} or 10^{-30} in some cases. This level of out-of-band signal rejection is confirmed by the Zodiacal light data described below.

4.1.1. Zodiacal Light Verification

As mentioned above, optical filters are used to prevent out-of-band light from impinging on the HFI detectors and registering as signal. While these filters are thoroughly characterized and tested before flight, it is of interest to try to confirm, as well as possible, their behavior in situ. In this section, the HFI observations of the Zodiacal light, specifically 100 GHz data, are used to place an upper limit on out-of-band spectral contribution, i.e., spectral leaks. The spectral profile of Zodiacal emission is well understood (e.g., Kelsall et al. (1998)), with Zodiacal emission much brighter in the mid-infrared than in the millimeter wavelength range and very little Zodiacal-correlated signal observed at 100 GHz (Fixsen & Dwek 2002). While the Diffuse Zodiacal Cloud is observed in the higher-frequency HFI channels (Planck Collaboration XIV 2013), it is not detected within the lower frequency HFI channels. A model Zodiacal light spectral emission profile is shown in Figure 18, with a dashed line representing the reduced emissivity for frequencies less than 2 000 GHz, as expected.

To set limits on a hypothetical leak at short wavelengths, the curve in figure 18 is frequency integrated to find the expected Zodiacal cloud emission flux density. To estimate the expected in-band flux density, an in-band emissivity of approximately 0.041 (see Planck Collaboration XIV (2013)) is coupled with the Zodiacal emission profile at an effective blackbody temperature of 286 K ($Z_{100\ \mathrm{GHz}}$ below). This is combined with the nominal 100 GHz channel bandwidth ($\Delta\nu_{100\ \mathrm{GHz}}$ below, approximately 33 GHz), where the product yields the expected in-band Zodiacal signal. This product is then divided by the total Zodiacal flux density estimated by the frequency integration of the Zodiacal spectral profile. Thus, an upper limit on any 100 GHz high frequency spectral leakage, L_{U}, is given by:

$$L_{\mathrm{U}} < \frac{Z_{100\ \mathrm{GHz}} \cdot \Delta\nu_{100\ \mathrm{GHz}}}{\int_{\nu_1}^{\nu_2} d\nu \cdot I(\nu)} < 1.2 \cdot 10^{-8} \quad . \tag{37}$$

The frequency range used in the above integration is 3 THz – 150 THz (equivalent to 100 μm – 2 μm). This integration region covers the dominant signal and is well above the 100 GHz band cut-off. Differences in the integration between this range and larger ones result in changes to the spectral leak upper limit at the sub-percent level, and thus do not effect the calculation at the desired accuracy.

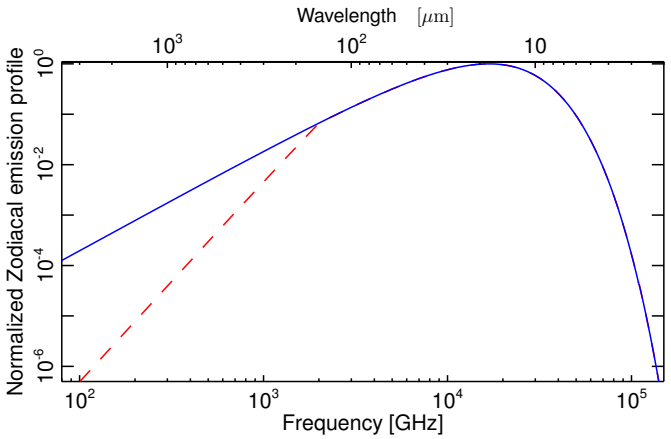

Fig. 18. The spectrum of the diffuse cloud in the Ecliptic plane. The blue curve represents the spectrum one would see assuming that uniform cloud emissivity of unity. The dotted red line shows the modification expected with a $1/\lambda^2$ emissivity proportionality for frequencies below 2 000 GHz (i.e., wavelengths longer than 150 μm).

The lack of any *Planck* detection of the Diffuse Zodiacal cloud signal at 100 GHz (Planck Collaboration XIV (2013)), indicating high out-of-band Zodiacal signal rejection, thus places confidence in the out-of-band signal discrimination of the HFI detector optical filters. Through this analysis, out-of-band discrimination has been shown to be greater than 10^8 for the HFI 100 GHz detectors. Less stringent limits can be set on smaller subsets of the band including wavelengths greater than 100 μm.

4.2. Bandpass Missmatch

Variations of the spectral response of individual detectors from the band-average response can be compared with similar variations in HFI data. An example of this is the observation of CO emission within some of the HFI bands. As CO emission is intrinsically narrow-banded, differences in CO sensitivity for different HFI detectors are easily compared to the HFI spectral response variations. Other components of the sky signal may also be used to perform similar comparisons (e.g., SZ, polarization leakage, dust, etc.).

Polarization leakage is an effect where spectral mismatch between detectors in the same frequency band induces a reduction/loss in an unpolarized intensity map and an over-estimation of the corresponding polarization map. This effect, which is a result of the assumptions required within the mapmaking algorithms, can also cause polarization to intensity leakage, but this is of less concern, however, due to relatively weak amplitudes of polarization signals coupled with the low levels of leakage expected. While a discussion of the polarization aspects of the HFI spectral response will be withheld until the release of *Planck* polarization data, the concept is introduced here to provide context to the current work as the same effect that causes polarization leakage allows a sky-based estimate of the respective colour correction / unit conversion coefficients (see Sect. 4.2.2).

4.2.1. CO Bandpass Verification

Analysis of HFI data, using component separation methods that include a CO emission component (Planck Collaboration XIII (2013) and Planck Collaboration XII (2013)), has provided all-sky maps of CO emission for the first three CO rotational transitions, i.e., CO J=1→0, CO J=2→1, and CO J=3→2. Select molecular cloud regions with well-known CO emission properties provide external validation of the HFI CO maps. One of the validation observations used was the DAME survey (Dame et al. 2001), which observed the CO J=1→0 transition. As the HFI CO maps are the result of component separation performed on maps in K_{CMB} units, and the external CO observations are typically available in units of velocity integrated brightness temperature, i.e., $K\,km\,s^{-1}$, this allows for a sky-based estimate of the CO unit conversion coefficients from units of $K\,km\,s^{-1}$ to units of K_{CMB}. These coefficient estimates are then compared against the bandpass-based coefficients, i.e., those based on the pre-flight measured spectral transmission data and the respective unit conversion relation above (Eq. 36). Another benefit of comparing the bandpass and sky-based CO results is the potential for improved understanding of systematic uncertainties in the bandpass data.

While a detailed discussion regarding the derivation of the sky-based CO unit conversion coefficients is found elsewhere (Planck Collaboration XIII 2013), this work discusses only those details relevant to the comparison of the sky and bandpass CO coefficients. The bandpass CO coefficients provide a direct conversion from differential CMB emission to that of CO, with the caveat that a precise knowledge of the CO unit conversion coefficients from the bandpass data is difficult to obtain in that the spectral resolution of the bandpass data is much broader than any observed CO emission features. Thus, the bandpass CO coefficients are an estimate based upon under-resolved spectroscopic measurements. The sky-based CO coefficients, on the other hand, provide a relative conversion coefficient based on the variation in spectral transmission between detectors within a common frequency band.

The linear combination method of CO signal extraction used to obtain the HFI CO products involves using a weighted sum derived to maximize the contrast between the desired component and its residuals (see Hurier et al. (2010) for details). Within the use of this method in the CO extraction, the DAME data set is used as a calibration template for the weighted map sums within a frequency band (i.e., the *Planck* 100, 217, or 353 GHz bands).

As demonstrated in Eqs. 1 and 5 of Planck Collaboration XIII (2013), the weighted coefficient for an individual detector signal is given by $w_i F_i$, where w_i is the `MILCA` relative weight, and F_i is the CO unit conversion coefficient. For the sky-based CO coefficients, the coefficient estimate is based upon the correlation of the CO component separation output with the DAME survey; thus, the relative CO and CMB weighting of the bandpass spectra (i.e., the numerator and denominator of Eq. 36) are determined indirectly, without the bandpass data. To illustrate the difference between the relative transmission at the CO rotational transition frequencies (e.g., just the numerator of Eq. 36), and the relative unit conversion for the CO transitions (e.g., all of Eq. 36), Fig. 19 compares these two sets of parameters. Although the two relative values demonstrate a correlation, they do not demonstrate perfect agreement. It is therefore important that CO unit conversion coefficients account for both the relative differences in spectral transmission at the CO rotational transition frequencies as well as the relative spectral transmission variations within the CMB signal over the entire band of a given detector.

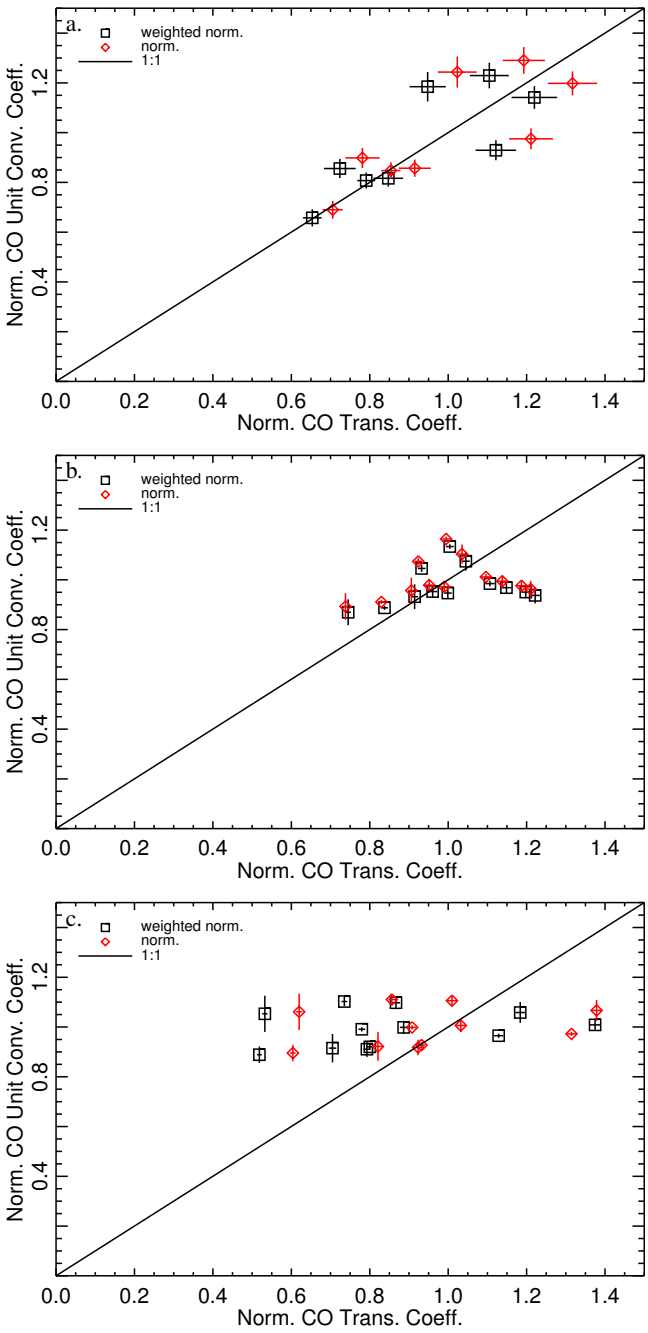

Fig. 19. A comparison of the relative spectral transmission at the CO transition frequency with the relative CO unit conversion coefficient for the 100 (a.), 217 (b.), and 353 (c.) GHz bands.

Through modeling of CO emission in a molecular cloud as a function of CO rotation temperature, it can be shown that the relative line intensities vary with CO rotation temperature, where the lower order transitions dominate for very low temperatures (e.g., less than 10 K). As the relative line intensity for, e.g., the CO J=2→1 and CO J=1→0 transitions varies with temperature, and the lowest CO transition is used in the HFI/DAME CO map calibration, the uncertainty of the HFI CO maps is expected to vary with CO temperature. This is consistent with the uncertainty varying with the observed CO intensity. Thus, in comparing the sky and bandpass CO coefficients, it is important to note that the relative intensities of CO emission change with CO rotational temperature and that for the higher order rotational tran-

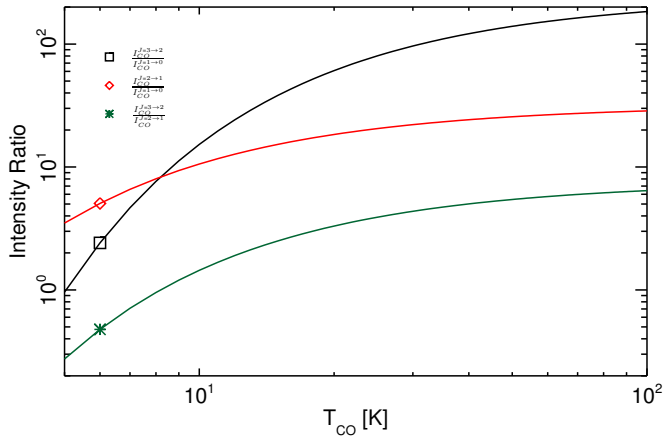

Fig. 20. Comparison of the relative CO specific intensity for the first three rotational transitions, for a varied CO rotation temperature. The normalization employed removes any dependence on the column density.

sitions, the sky CO coefficients are a generalized scalar value representing a dynamic quantity.

The sky-based coefficients do not provide a conversion that includes an absolute calibration, but represent the relative levels between detectors of the same frequency band; the absolute calibration comes from the external data sources used for validation. This is a result of the linear combinations used in combining detector signals in such a way as to enhance certain spectral components while reducing other spectral contaminants (Hurier et al. 2010).

Another difference between the sky/DAME and bandpass CO coefficients is the isotopic content of the calibration. The sky-based coefficients provide an estimate of CO emission from all isotopic species, while the bandpass CO coefficients are calculated for isotopic contributions individually (e.g., the emission frequencies vary with isotope). The bandpass coefficients for individual isotopes could be combined provided information regarding the isotopic ratios were available for a given region. Thus, there is a normalization/rescaling step needed to compare the two values, and a complete comparison is unconstrained at present without additional calibration data.

Additionally, the sky-based coefficients are based on unpolarized intensity, so the PSB detector pairs are combined in the form $(A + B)/2$ to reduce the influence of any polarized signal. Any uncertainty in the data introduced as a result of this step must be propagated through to the sky CO coefficients.

For these reasons the sky and bandpass CO coefficients are expected to show a correlation, but are not expected to exhibit perfect agreement. This is particularly true of an absolute comparison; relative differences should be proportionate, but the absolute values of the bandpass and sky coefficients are not expected to be directly compatible (Planck Collaboration XIII 2013).

Efforts were taken to understand the accuracy of the bandpass CO coefficients in light of the differences observed between the sky and bandpass CO coefficients. As demonstrated in Eq. 36, the relative spectral transmission over a very narrow frequency range, in principle a delta function, is needed in order to obtain a CO unit conversion coefficient. This ideally requires knowledge of the HFI spectral response to much finer spectral resolution than is available. Each of the other unit conversion and colour correction calculations are based on relatively broad spectral features that are not dominated by uncertainties within just one spectral bin. Thus, it is difficult to ensure that the nominal transmission and uncertainty for a single spectral bin are consistent with the values provided within the detector bandpass data. In order to investigate the effects of CO transmission interpolation and uncertainty errors on the CO conversion coefficients, the bandpass CO coefficients were repeatedly calculated after varying levels of smoothing were applied to the data. Smoothing was done in steps of one from one to nine. The smoothing results in noise averaging within an increasingly broad spectral bin width, so the intrinsic spectral transmission uncertainty is reduced, but the interpolation error may be increased. Fig. 21 illustrates the changes in CO coefficients upon introduction of this spectral smoothing. It is evident that the spread in coefficient values with smoothing factor is greater than the coefficient uncertainty in many cases. Thus, the bandpass CO coefficients have been revised to include this result. Within the Planck Collaboration XIII (2013) paper, this is reflected as an increase in the error bars of the bandpass CO coefficients.

Another check performed on the bandpass CO coefficients was the introduction of a linear slope to the detector spectra, as described in Sect. 3.2.3 and demonstrated in Fig. 16 for a combined unit conversion and dust colour correction. As was found to be the case above, the addition of a linear slope to the spectra resulted in a linear change in the CO coefficients. In this instance the changes observed in the CO coefficients were well within the quoted uncertainty, so the uncertainty is not underestimated in this respect. Fig. 22 illustrates the shift in CO coefficients caused by the introduction of a linear scaling of the spectra.

The variation between the sky-based and bandpass-based CO unit conversion coefficients is demonstrated in Figs. 23 – 24 for the HFI 100, 217, and 353 GHz channels. The first figure indicates the correlation between the normalized sky and bandpass coefficients, while the second shows the sky and bandpass coefficients grouped together about their respective feed horns. Plotting the sky coefficients on this scale required scaling the relative sky coefficients about the bandpass coefficient mean. This was done to allow comparison with the ^{13}CO coefficients as well as the ^{12}CO coefficients (Fig. 24 also includes the ^{13}CO coefficients although these were not used in the sky coefficient scaling). The ^{13}CO coefficients are expected to have a stronger influence on the 100 GHz channel than for the higher frequency channels (Planck Collaboration XIII 2013). The plots indicate the detector type as either the individual PSB detectors (A and B separately), the combined PSB detectors ($(A + B)/2$), or the spiderweb (SWB) detectors. Although this comparison is underconstrained, and the two sets of coefficients do not represent exactly the same quantity, as has been discussed above, there is a general agreement between the sky-based and bandpass-based CO coefficients. The CO analysis also required a dust template as part of the component separation. Thus, a sky-based estimate of HFI dust colour correction coefficients was a by-product of this analysis. There is excellent agreement found between the bandpass- and CO/sky-based dust colour correction coefficients; more details on this are provided in Sect. 4.2.2, with the results presented in Fig. 28.

There remain differences in the sky- and bandpass-based CO unit conversion coefficients. The analysis of CO data in the 2013 *Planck* data release is based upon the sky-based CO coefficients. The differences between the two approaches are acceptable for present analysis, but are increasingly important for future work, including the analysis of *Planck* polarization data. Thus, while there is a correlation between the two approaches, a better understanding of these differences is required to gain a deeper under-

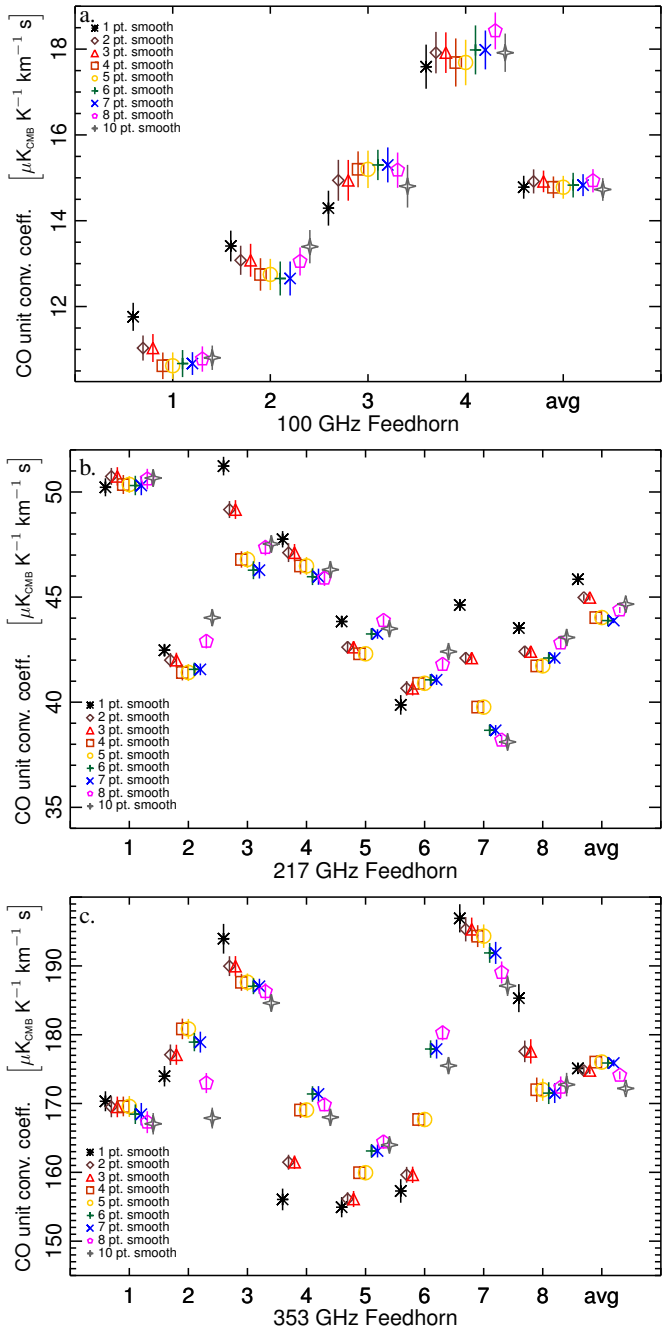

Fig. 21. Comparison of the CO unit conversion coefficients with a smoothing / re-binning factor applied to the spectra going in to the unit conversion algorithm, for the 100 (a.), 217 (b.), and 353 (c.) GHz detectors.

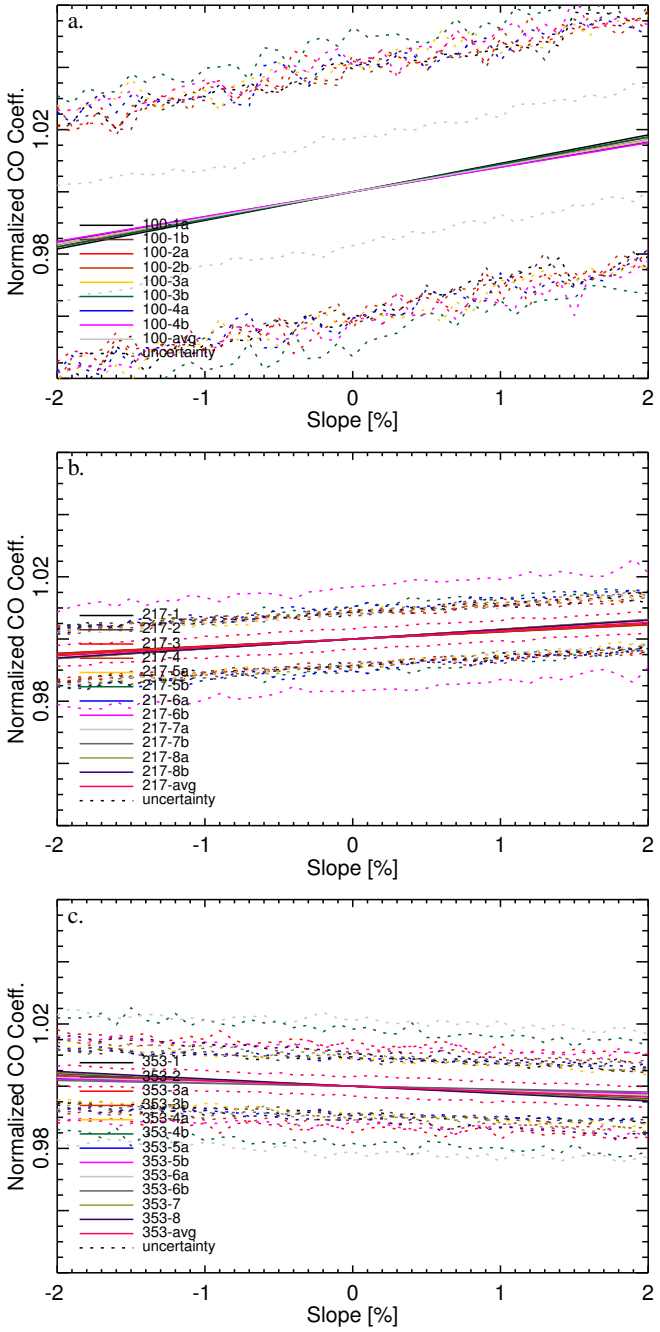

Fig. 22. Comparison of CO unit conversion coefficients with an additional linear scaling of the input spectra, for the 100 (a.), 217 (b.), and 353 (c.) GHz detectors.

standing of the *Planck* data. This comparison presents the current standing of a work in progress.

4.2.2. Dust Colour Correction Bandpass Verification

As a result of work investigating polarization leakage, a study was conducted to estimate the on-sky integration of dust SEDs for dusty regions directly using flight data, i.e., without using the spectral transmission data. This was done to investigate the compatibility of the two methods.

To derive the dust spectral mismatch for a given HFI frequency band, dust colour correction coefficients for each individual detector must be known for the bolometers/detectors within the given band. Differences between the dust content of individual bolometer maps and the corresponding frequency channel map can be used to estimate these coefficients. In performing this analysis, care must be taken to understand all of the spectral components included in the maps (e.g., CMB, free-free, CO, etc.), and calibration errors, beam errors and beam differences, and any residual polarization signal within the bolometer intensity maps.

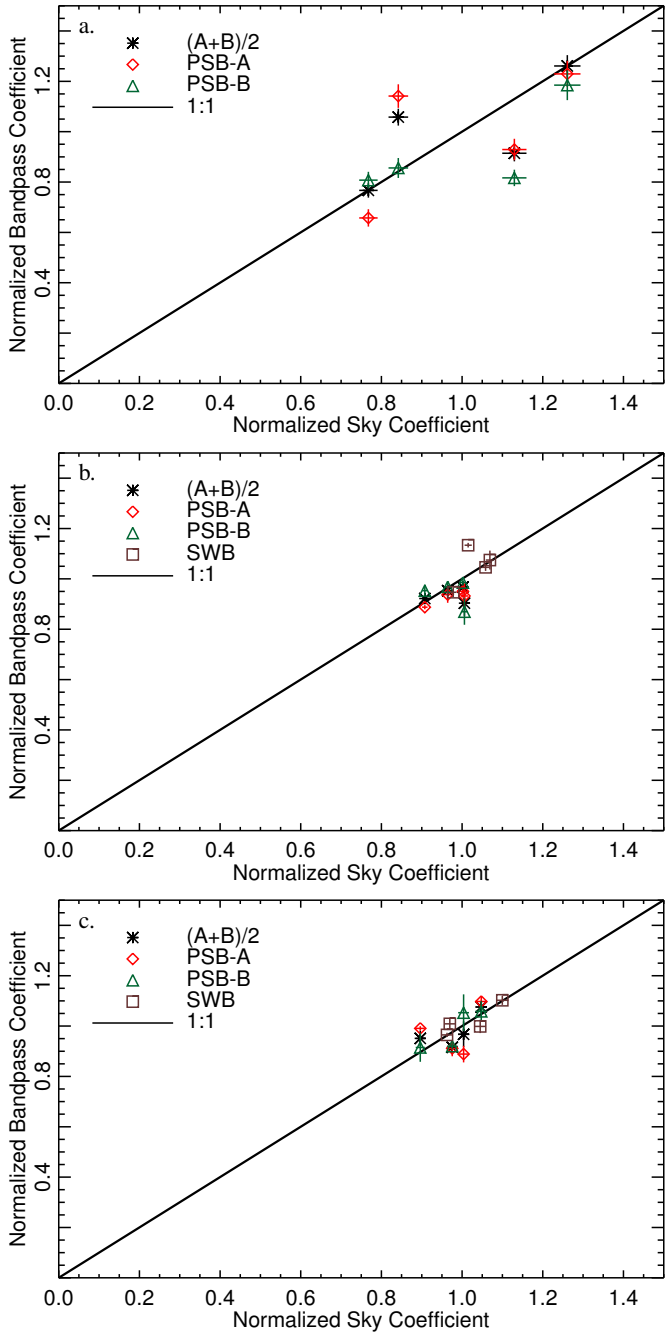

Fig. 23. Relationship between the CO unit conversion coefficients based on the CO-sky maps and the spectral response data for the CO J=1→0 transition within the 100 GHz HFI band (top), the CO J=2→1 transition within the 217 GHz HFI band (middle), and the CO J=3→2 transition within the 353 GHz HFI band (bottom).

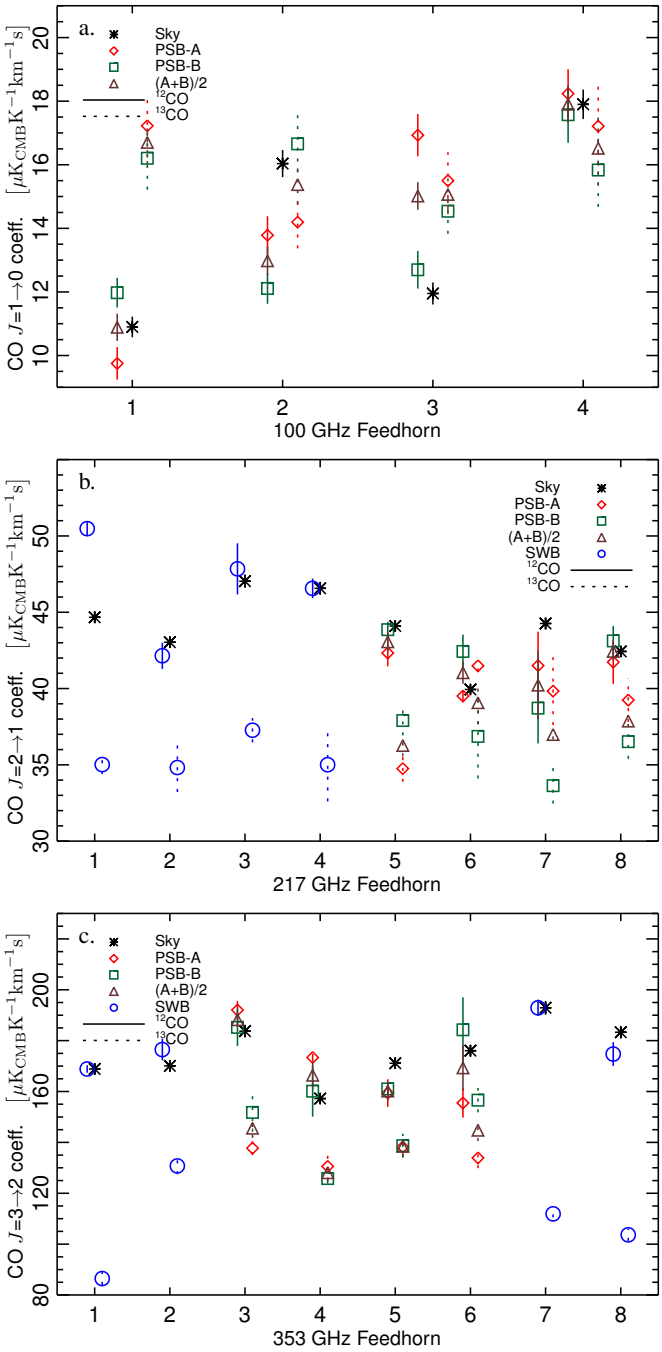

Fig. 24. Comparison of CO unit conversion coefficients, scaled about the bandpass coefficient amplitudes for the sky and bandpass coefficients. This scaling allows comparison with both the ^{12}CO and ^{13}CO bandpass coefficients; the bandpass isotopic coefficients are horizontally offset in opposing directions for clarity.

To avoid polarization bias, the study was restricted to regions surrounding the ecliptic poles, where there is a large variety in the crossing angles for multi-scan observations of a given region with a single detector. Stokes I, Q, and U maps were produced for individual detectors in addition to the standard I, Q, and U frequency channel maps nominally produced by the data pipelines.

From the ecliptic polar maps, there were three regions selected for this study, all specifically selected for their relative component/content differences. The Large Magellanic Cloud (LMC, (l,b)=(280.°5, -32.°8), Planck Collaboration XVII (2011)) was selected as a familiar target with known dust properties. Another source selected was a region slightly North of the LMC in the Chamealeon constellation (CHA, (l,b)=(287.°6, -24.°1)), and the final region used in this study was near the North Ecliptic Pole (NEP, (l,b)=(103.°0, 18.°8)). For each of the HFI frequency bands, and all of the individual detectors, square maps of 13°

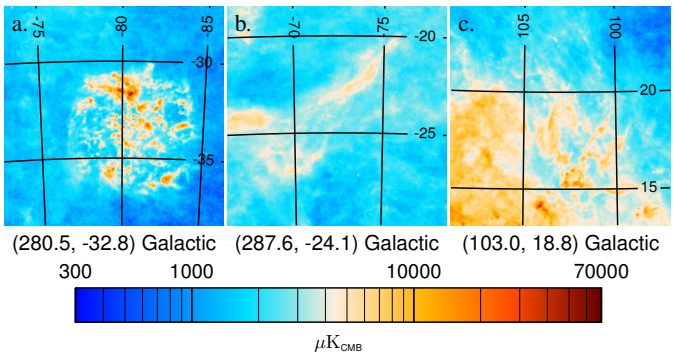

Fig. 25. 353 GHz maps of the ecliptic polar maps for the LMC (left), CHA (middle), and NEP (right) regions of the sky.

width, with 4′ pixel resolution, were extracted from the I, Q, and U maps described above. The dust SED properties of the LMC from a previous *Planck* publication are $T_D = 21.0 \pm 1.9$ K and $\beta = 1.48 \pm 0.25$ (Planck Collaboration XVII (2011)); as the sky-based dust colour correction coefficients for all sources remain consistent (see Fig. 28), the LMC dust properties and uncertainties mentioned above are used to determine the bandpass coefficients included in this section of this work, along with their respective uncertainty. Fig. 25 provides the HFI observations over these regions at 353 GHz. The corresponding band-average unit conversion / colour correction coefficient maps (see Sect. 3.4) for each band were used to verify the uniformity of the expected band-average colour correction across these regions of the sky. While Fig. 17 provides examples of full-sky band-average coefficient maps, Fig. 26 provides a similar example over the three specified sky regions used in the sky/bandpass dust colour correction coefficient comparison. The changing level of coverage between surveys is especially apparent for the NEP region. Histograms of these band-average coefficients for the full sky and dusty regions are provided in Fig. 27.

A component separation is performed to isolate CMB, free-free, CO, and dust emission from the 100, 143, 217, and 353 GHz frequency channels. Regions of high free-free and high CO emission are masked in the dust maps, leaving residual maps primarily containing CMB and dust. The CMB signal is removed by subtracting the frequency-band map from the individual detector maps as described below. Let U_D represents the dust colour correction for the frequency-band map of a given channel, and let $U_{D\,i}$ represent the individual bolometer dust colour correction coefficient. The intensity map, I, for the channel will thus be given by $I = C + U_D D$, where C is the CMB component, and D is the dust component (note: C and D represent the actual observable intensity, not just what the detector sees). The detector intensity map will be given by $I_i = C + U_{D\,i} D$. The regression coefficient resultant from the correlation of the difference map $I_i - I$ with the channel map I can be used to derive the *relative* dust colour correction coefficient as follows:

$$I_i - I = (U_{D\,i} - U_D)D \quad , \tag{38}$$

$$\mathrm{Corr}\,(I_i - I, I) = \frac{U_{D\,i} - U_D}{U_D} \quad , \tag{39}$$

$$\frac{U_{D\,i}}{U_D} = \mathrm{Corr}\,(I_i - I, I) + 1 \quad . \tag{40}$$

Thus the relative dust colour correction coefficient may be determined for each individual HFI detector by employing the above relation. It is important to note that the dust colour correction

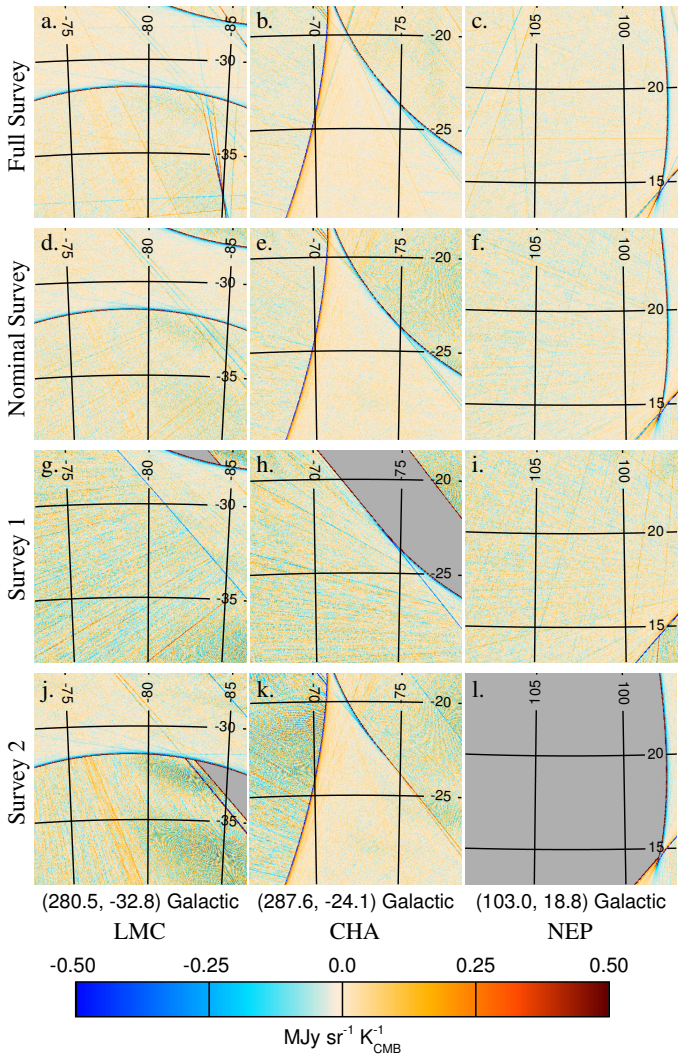

Fig. 26. 353 GHz maps of dust band-average unit conversion / colour correction (see Sect. 3.4). the maps show the deviation in the combined unit conversion / colour correction from the full-sky map median values. The full-sky median coefficient values, i.e., offsets, used for the Full (a.,b.,c.), Nominal (d.,e.,f.), First (g.,h.,i.), and Second (j.,k.,l.) surveys are, 278.980, 278.970, 278.960, and 278.970 MJy sr^{-1} K_{CMB}, respectively. The figure columns represent the ecliptic polar maps for the LMC (a., d., g., and j.), CHA (b., e., h., and k.), and NEP (c., f., i., and l.) regions of the sky.

coefficients in the above expression convert from the dust spectral profile to the CMB spectral profile; in the notation of the HFI unit conversion and colour correction syntax, this is equivalent to the inverse (i.e., U_D^{-1}) of a colour correction from the dust spectral profile to a powerlaw spectral index of -1 *followed* by a unit conversion from a powerlaw spectral index of -1 to differential CMB temperature units.

Fig. 28 illustrates the excellent agreement between the sky-based Dust colour correction coefficients and those based on the HFI spectral response (i.e., Eq. 32 and 35) for the 100, 217, and 353 GHz spectral bands. This level of agreement is not found amongst the 143 GHz detectors, however. The source of this discrepancy is under investigation. It should be noted that the dust

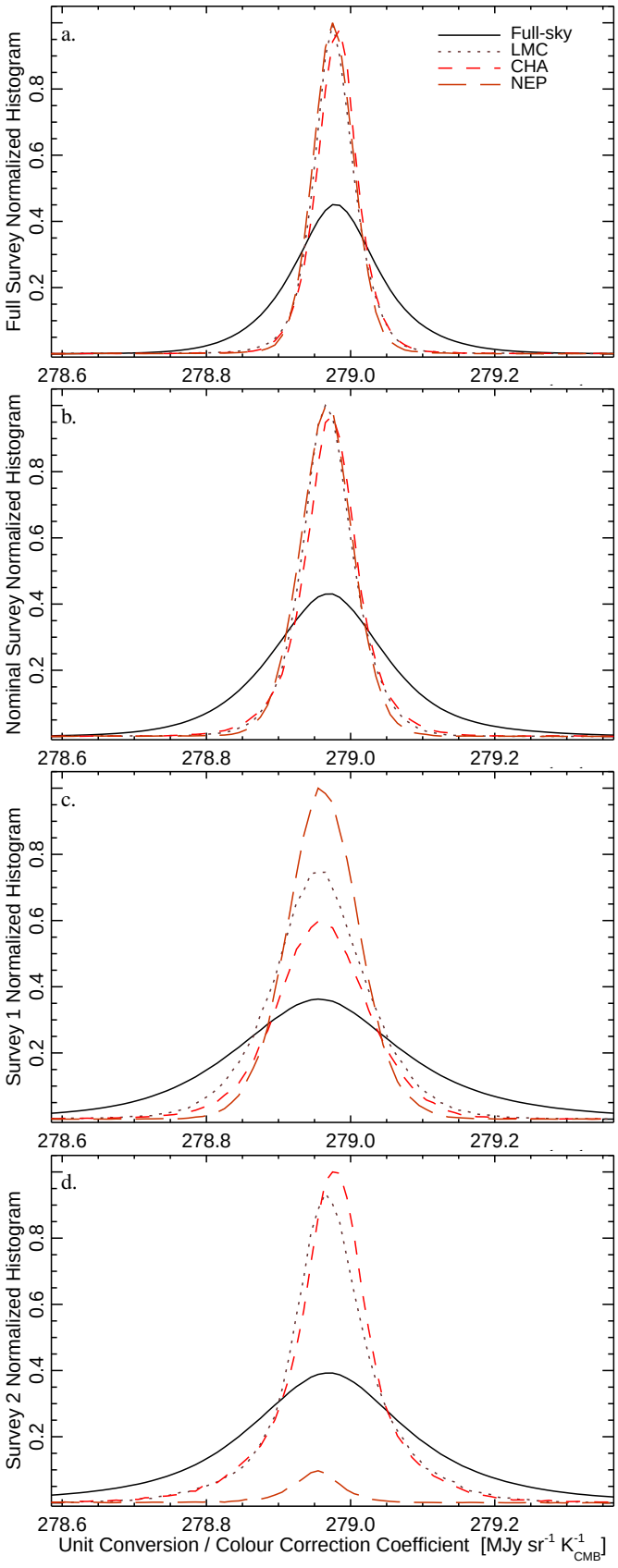

Fig. 27. Histograms of the 353 GHz dust unit conversion / colour correction maps for the Full survey (a.), Nominal survey (b.), survey 1 (c.) and survey 2 (d.). The plots include histograms based on the full sky as well as the LMC, CHA, and NEP regions.

emission is much stronger with higher frequencies, and is thus less dominant at 143 and 100 GHz.

A dust colour correction coefficient originating from the CO extraction (Planck Collaboration XIII 2013) is also shown for the 217 and 353 GHz bands.

The 217 and 353 GHz portions of Fig. 28 also contain data points from the CO extraction (Planck Collaboration XIII 2013). The horizontal bars on some of these points indicate that the coefficient was derived for the PSB A/B pair of detectors, not the detectors individually. For the 217 and 353 GHz coefficients, the bandpass and CO values are in excellent agreement, even where the dust coefficients from this study appear to diverge from the bandpass values slightly. The exact causes of these variations remains under study for a future data release.

The uncertainty in the figures for the sky-based dust coefficients is based on an absolute calibration uncertainty of 0.5 % for each band. The bandpass based coefficient uncertainties are based upon the quoted uncertainties of $T_{\rm D}$ and β of 1.9 K and 0.25, respectively, as well as the spectral uncertainty associated with each spectral response profile. The CO coefficient uncertainties are based upon a 1 % relative calibration uncertainty.

4.2.3. S-Z Bandpass Verification

The Sunyaev-Zeldovich (SZ) effect (Sunyaev & Zeldovich 1980) has a characteristic signature in the millimetre/ submillimetre domain. With a changing sign at 217 GHz, it is quite different from the CMB anisotropy spectrum and other power-law spectra typical of these frequencies. Consequently, any bandpass leakage should be clearly identifiable in SZ spectra. To isolate the SZ signature from other foregrounds and the CMB anisotropies themselves, the 20 brightest clusters in the Planck catalog (Planck Collaboration XXVIII 2013, Planck Collaboration XXIX 2013, and Planck Collaboration XXI 2013) have been selected to provide lines-of-sight over which to investigate spectral mismatch leakage. The lines-of-sight selected are A2319, A3266, RXC J1638.2-6420, A2219, A2142, Coma, A366, A2255, A2029, A3186, A2218, A3158, A85, A3827, A697, A1795, A644, A2204, A3628, and A3888. For each of the above sources, the integrated flux in individual HFI channel maps is measured (calibrated in thermodynamic temperature $\rm K_{CMB}$ units) at the position of each cluster. Using the nominal bandpass conversion coefficients for each of the expected components, the integrated $Y_{\rm SZ}$ for each cluster is deduced from the residuals using a χ^2 statistical analysis. Thus, an estimate of the SZ unit conversion from the $Y_{\rm SZ}$ Compton parameter to the $dT_{\rm CMB}$ differential CMB temperature may be obtained for each cluster, and each frequency; without invoking the bandpass-based SZ unit conversion coefficients themselves (Eq. 33, Table 6). This analysis provides a consistency check of the bandpass-based SZ coefficients.

Two methods have been used to perform this analysis. The first allows only a dust template removal, fixed on the 857 GHz channel, with coefficients deduced outside each cluster. This first method does not make assumptions about the colour of the background. The background removal was accomplished via subtraction of an average value taken on an annulus surrounding the cluster, i.e., aperture photometry. This method has a low signal-to-noise ratio because it is dominated by the CMB anisotropy residuals. The second method uses the `MILCA` algorithm (Hurier et al. 2010) to subtract a component with a CMB spectrum at all frequencies. The average of these coefficients per frequency is shown in Table 8 for the two methods and compared with the expected coefficients based on the nominal band-average transmis-

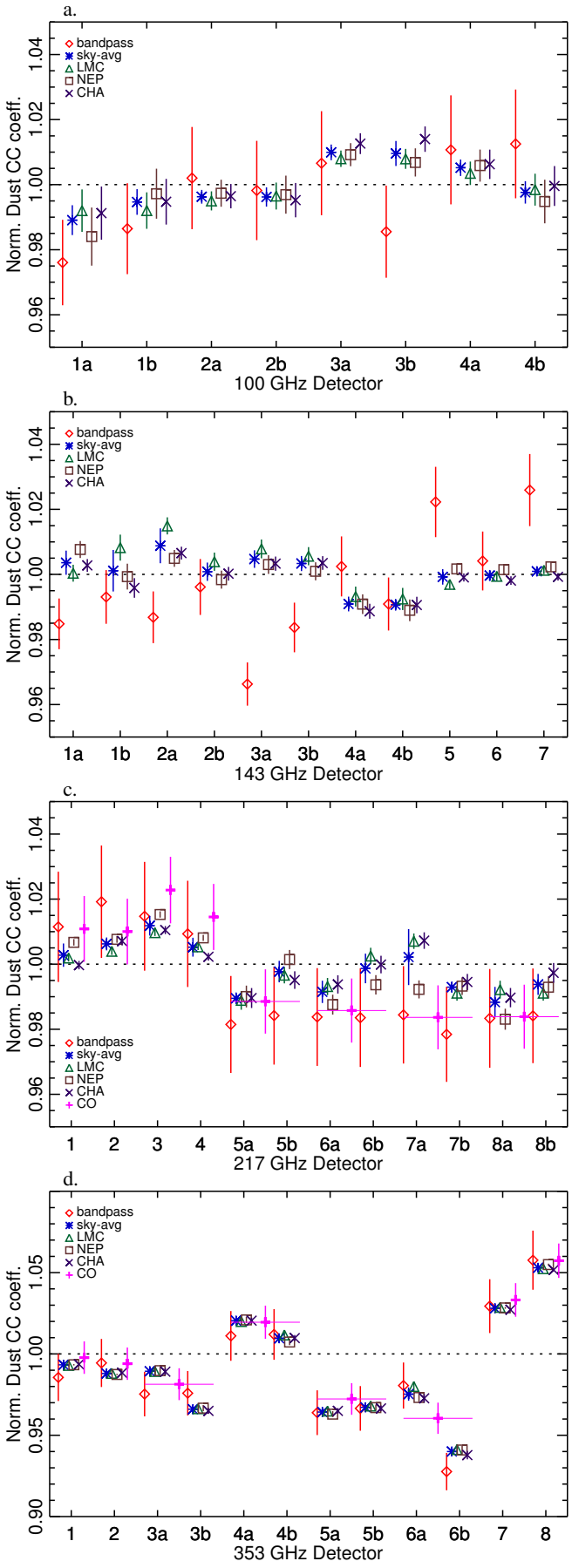

Fig. 28. Comparison of the sky and bandpass based dust unit conversion / colour correction coefficients for the HFI 100 GHz – 353 GHz spectral bands (a. – d.).

Table 8. Various y_{SZ} to dT_{CMB} unit conversion factors.

Band [GHz]	$U_{c\,BP}$ [y_{SZ}/K$_{CMB}$]	$U_{c\,Ap.\,Phot}$ [y_{SZ}/K$_{CMB}$]	$U_{c\,MILCA}$ [y_{SZ}/K$_{CMB}$]
100	−4.030 ± 0.018	−4.7 ± 0.6	−4.6 ± 0.2
143	−2.78 ± 0.04	−3.9 ± 0.6	−3.00 ± 0.10
217	0.19 ± 0.05	−1.3 ± 0.6	−0.10 ± 0.10
353	6.21 ± 0.11	4.3 ± 0.8	5.6 ± 0.2
545	14.46 ± 0.07	17.4 ± 6	17 ± 2

sion spectra. Although the signal-to-noise ratio is not larger than typically 10 for the first method and 30 for the second method, the agreement is remarkable. Thus, the SZ cluster data provides a pseudo-quantitative verification of the accuracy of the HFI detector spectra as gross spectral leakages would demonstrate themselves through this analysis.

5. Conclusions

The spectral response for the HFI detectors has been presented. The derivation of the HFI frequency channel band-average spectra has been presented, including photometric/noise/sky coverage constituent scaling coefficients. The scaling coefficients for the band-average spectra were compared with those resulting from the various individual HFI surveys, where it was demonstrated that the individual survey values converged to the full survey average values used in the derivation of the spectral response data products. Unit conversion and colour correction coefficient relations have been derived. The corresponding coefficients, and uncertainties, are to be made available within the *Planck* data archive (Planck Collaboration ES 2013). The accuracy of the HFI spectral response has been verified using both ground-based component level data and, importantly, HFI flight data. The defining requirement indicated in the original HFI calibration plan is knowledge of the spectral transmission of the individual detectors with uncertainties below 3 % for the low frequency channels (100, 143, and 217 GHz) and below 1 % for the high frequency channels (353, 545, and 857 GHz); all with a spectral resolution of better than 3 GHz. The spectral resolution requirement has been exceeded by more than a factor of five. It is possible to degrade the spectral resolution requirement to gain an improvement in the S/N, which allows the desired spectral transmission accuracy to be achieved in most cases (the absolute uncertainty for the 100 GHz detectors is high due to the high noise levels of the reference bolometer at these frequencies, but the relative uncertainty even for the 100 GHz detectors remains low). Estimates of the out-of-band transmission profiles have been incorporated into the bandpass data products. Out-of-band signal attenuation is demonstrated to be better than 10^8 through HFI observations of the diffuse zodiacal cloud Planck Collaboration XIV (2013). Good agreement has been demonstrated between sky and bandpass dust colour correction coefficients, as well as SZ unit conversion coefficients. The sky and bandpass based CO coefficients have shown a correlation, yet a full comparison is unconstrained at this time due to differences between the two approaches. The CO comparison is a work in progress, where improvements are expected as *Planck* polarization data analysis progresses. Software tools to calculate *Planck* unit conversion and colour correction coefficients have been provided, along with tables of coefficient values for individual de-

tectors, and band-average spectra, in Planck Collaboration ES (2013).

Acknowledgements. The authors wish to thank Emmanuel Lellouch, Raphael Moreno, and Matt Griffin for the provision of the planet model spectra used to generate HFI planet colour correction coefficients. The corresponding author acknowledges funding support for this work from NSERC and the Canada-United Kingdom Millennium Research Award program as well as the STFC (UK). The development of *Planck* has been supported by: ESA; CNES and CNRS/INSU-IN2P3-INP (France); ASI, CNR, and INAF (Italy); NASA and DoE (USA); STFC and UKSA (UK); CSIC, MICINN, JA and RES (Spain); Tekes, AoF and CSC (Finland); DLR and MPG (Germany); CSA (Canada); DTU Space (Denmark); SER/SSO (Switzerland); RCN (Norway); SFI (Ireland); FCT/MCTES (Portugal); and PRACE (EU). A description of the Planck Collaboration and a list of its members, including the technical or scientific activities in which they have been involved, can be found at http://www.sciops.esa.int/index.php?project=planck&page=Planck_Collaboration. The author list for this paper has been selected by the *Planck* Science Team from the Planck Collaboration, and is composed of individuals from all of the above entities who have made multi-year contributions to the development of the mission.

References

Ade, P. A. R., Savini, G., Sudiwala, R., et al. 2010, A&A, 520, A11+
Beichman, C. A., Neugebauer, G., Habing, H. J., Clegg, P. E., & Chester, T. J., eds. 1988, Infrared astronomical satellite (IRAS) catalogs and atlases. Volume 1: Explanatory supplement, Vol. 1
Bell, R. J. 1972, Introductory Fourier Transform Spectroscopy (New York: Academic Press)
Born, M. & Wolf, E. 1999, Principles of Optics: Electromagnetic Theory of Propagation, Interference and Diffraction of Light, seventh edn. (Cambridge University Press)
Brault, J. W. 1987, Mikrochimica Acta, 3, 215
Catalano, A. 2008, PhD thesis, IAP, Paris, title Translation: Development of numerical models of the High Frequency Instrument (HFI) of Planck necessary for its operation
Catalano, A., Coulias, A., Recouvreur, G., & Lamarre, J. 2006, HFI Calibration Report – EFF Sequences, Tech. Rep. 01-00, Observatoire de Paris, filename: EFF_Calibration.pdf
Connes, J. 1961, Rev. Opt., 40, 45, 116, 171, 233, english translation as document AD 409869, Clearinghouse for Federal Scientific and Technical Information, Cameron Station, VA.
Dame, T. M., Hartmann, D., & Thaddeus, P. 2001, ApJ, 547, 792
Davis, S. P., Abrams, M. C., & Brault, J. W. 2001, Fourier Transform Spectroscopy, 1st edn. (Academic Press)
Fixsen, D. J. 2009, ApJ, 707, 916
Fixsen, D. J. & Dwek, E. 2002, ApJ, 578, 1009
Forman, M. L., Steel, W. H., & Vanasse, G. A. 1966, Journal of the Optical Society of America, 56, 59
Górski, K. M., Hivon, E., Banday, A. J., et al. 2005, ApJ, 622, 759
Grainger, W. 2001, PhD thesis, University of Cambridge
Griffin, M., North, C., Amaral-Rogers, A., et al. 2013, MNRAS, In Press, submitted Feb. 2013.
Holmes, W. A., Bock, J. J., Crill, B. P., et al. 2008, Appl. Opt., 47, 5996
Hurier, G., Hildebrandt, S., & Macias-Perez, J. 2010, arXiv preprint arXiv:1007.1149
Jet Propulsion Laboratory, C. I. o. T. 2004, Molecular Spectroscopy Catalog, http://spec.jpl.nasa.gov/
Kelsall, T., Weiland, J. L., Franz, B. A., et al. 1998, ApJ, 508, 44
Kompaneets, A. S. 1957, Soviet Phys.-JETP, 4, 730
Lamarre, J., Puget, J., Ade, P. A. R., et al. 2010, A&A, 520, A9+
Maffei, B., Noviello, F., Murphy, J. A., et al. 2010, A&A, 520, A12+
Murphy, J. A., Peacocke, T., Maffei, B., et al. 2010, Journal of Instrumentation, 5, T04001
Naylor, D. A., Gom, B. G., Jones, S. C., & Spencer, L. D. 2009, in Spring Optics and Photonics Congress Fourier Transform Spectroscopy Topical Meeting (Optical Society of America), JTuB15
Naylor, D. A. & Tahic, M. K. 2007, J. Opt. Soc. Am. A, 24, 3644
Nyquist, H. 1928, Transactions of the American Institute of Electrical Engineers, 47, 617
Pajot, F., Ade, P. A. R., Beney, J., et al. 2010, A&A, 520, A10+
Planck Collaboration. 2013, Submitted to A&A
Planck Collaboration ES. 2013, The Explanatory Supplement to the Planck 2013 results (ESA)
Planck Collaboration I. 2013, Submitted to A&A
Planck Collaboration II. 2013, Submitted to A&A
Planck Collaboration VI. 2013, Submitted to A&A
Planck Collaboration VII. 2013, Submitted to A&A
Planck Collaboration VIII. 2013, Submitted to A&A
Planck Collaboration XII. 2013, Submitted to A&A
Planck Collaboration XIII. 2013, Submitted to A&A
Planck Collaboration XIV. 2013, Submitted to A&A
Planck Collaboration XIX. 2011, A&A, 536, A19
Planck Collaboration XVII. 2011, A&A, 536, A17
Planck Collaboration XXI. 2013, Submitted to A&A
Planck Collaboration XXIX. 2013, Submitted to A&A
Planck Collaboration XXVIII. 2013, Submitted to A&A
Planck HFI Core Team. 2011, A&A, 536, A6
Rosset, C., Tristram, M., Ponthieu, N., et al. 2010, A&A, 520, A13+
Rybicki, G. B. & Lightman, A. P. 1986, Radiative Processes in Astrophysics (New York: John Wiley & Sons)
Shannon, C. E. 1948, The Bell System Technical Journal, 27, 379
Sunyaev, R. A. & Zeldovich, I. B. 1980, ARA&A, 18, 537
Zonca, A., Franceschet, C., Battaglia, P., et al. 2009, Journal of Instrumentation, 4, 2010

[1] APC, AstroParticule et Cosmologie, Université Paris Diderot, CNRS/IN2P3, CEA/lrfu, Observatoire de Paris, Sorbonne Paris Cité, 10, rue Alice Domon et Léonie Duquet, 75205 Paris Cedex 13, France
[2] Aalto University Metsähovi Radio Observatory, Metsähovintie 114, FIN-02540 Kylmälä, Finland
[3] African Institute for Mathematical Sciences, 6-8 Melrose Road, Muizenberg, Cape Town, South Africa
[4] Agenzia Spaziale Italiana Science Data Center, c/o ESRIN, via Galileo Galilei, Frascati, Italy
[5] Agenzia Spaziale Italiana, Viale Liegi 26, Roma, Italy
[6] Astrophysics Group, Cavendish Laboratory, University of Cambridge, J J Thomson Avenue, Cambridge CB3 0HE, U.K.
[7] Astrophysics & Cosmology Research Unit, School of Mathematics, Statistics & Computer Science, University of KwaZulu-Natal, Westville Campus, Private Bag X54001, Durban 4000, South Africa
[8] Atacama Large Millimeter/submillimeter Array, ALMA Santiago Central Offices, Alonso de Cordova 3107, Vitacura, Casilla 763 0355, Santiago, Chile
[9] CITA, University of Toronto, 60 St. George St., Toronto, ON M5S 3H8, Canada
[10] CNRS, IRAP, 9 Av. colonel Roche, BP 44346, F-31028 Toulouse cedex 4, France
[11] California Institute of Technology, Pasadena, California, U.S.A.
[12] Centre for Theoretical Cosmology, DAMTP, University of Cambridge, Wilberforce Road, Cambridge CB3 0WA U.K.
[13] Centro de Estudios de Física del Cosmos de Aragón (CEFCA), Plaza San Juan, 1, planta 2, E-44001, Teruel, Spain
[14] Computational Cosmology Center, Lawrence Berkeley National Laboratory, Berkeley, California, U.S.A.
[15] DSM/Irfu/SPP, CEA-Saclay, F-91191 Gif-sur-Yvette Cedex, France
[16] DTU Space, National Space Institute, Technical University of Denmark, Elektrovej 327, DK-2800 Kgs. Lyngby, Denmark
[17] Département de Physique Théorique, Université de Genève, 24, Quai E. Ansermet,1211 Genève 4, Switzerland
[18] Departamento de Física Fundamental, Facultad de Ciencias, Universidad de Salamanca, 37008 Salamanca, Spain
[19] Department of Astronomy and Astrophysics, University of Toronto, 50 Saint George Street, Toronto, Ontario, Canada
[20] Department of Astrophysics/IMAPP, Radboud University Nijmegen, P.O. Box 9010, 6500 GL Nijmegen, The Netherlands
[21] Department of Electrical Engineering and Computer Sciences, University of California, Berkeley, California, U.S.A.
[22] Department of Physics and Astronomy, Dana and David Dornsife College of Letter, Arts and Sciences, University of Southern California, Los Angeles, CA 90089, U.S.A.
[23] Department of Physics and Astronomy, University College London, London WC1E 6BT, U.K.
[24] Department of Physics, Gustaf Hällströmin katu 2a, University of Helsinki, Helsinki, Finland

[25] Department of Physics, Princeton University, Princeton, New Jersey, U.S.A.
[26] Department of Physics, University of California, One Shields Avenue, Davis, California, U.S.A.
[27] Department of Physics, University of California, Santa Barbara, California, U.S.A.
[28] Department of Physics, University of Illinois at Urbana-Champaign, 1110 West Green Street, Urbana, Illinois, U.S.A.
[29] Dipartimento di Fisica e Astronomia G. Galilei, Università degli Studi di Padova, via Marzolo 8, 35131 Padova, Italy
[30] Dipartimento di Fisica e Scienze della Terra, Università di Ferrara, Via Saragat 1, 44122 Ferrara, Italy
[31] Dipartimento di Fisica, Università La Sapienza, P. le A. Moro 2, Roma, Italy
[32] Dipartimento di Fisica, Università degli Studi di Milano, Via Celoria, 16, Milano, Italy
[33] Dipartimento di Fisica, Università degli Studi di Trieste, via A. Valerio 2, Trieste, Italy
[34] Dipartimento di Fisica, Università di Roma Tor Vergata, Via della Ricerca Scientifica, 1, Roma, Italy
[35] Discovery Center, Niels Bohr Institute, Blegdamsvej 17, Copenhagen, Denmark
[36] European Southern Observatory, ESO Vitacura, Alonso de Cordova 3107, Vitacura, Casilla 19001, Santiago, Chile
[37] European Space Agency, ESAC, Planck Science Office, Camino bajo del Castillo, s/n, Urbanización Villafranca del Castillo, Villanueva de la Cañada, Madrid, Spain
[38] European Space Agency, ESTEC, Keplerlaan 1, 2201 AZ Noordwijk, The Netherlands
[39] Helsinki Institute of Physics, Gustaf Hällströmin katu 2, University of Helsinki, Helsinki, Finland
[40] INAF - Osservatorio Astrofisico di Catania, Via S. Sofia 78, Catania, Italy
[41] INAF - Osservatorio Astronomico di Padova, Vicolo dell'Osservatorio 5, Padova, Italy
[42] INAF - Osservatorio Astronomico di Roma, via di Frascati 33, Monte Porzio Catone, Italy
[43] INAF - Osservatorio Astronomico di Trieste, Via G.B. Tiepolo 11, Trieste, Italy
[44] INAF/IASF Bologna, Via Gobetti 101, Bologna, Italy
[45] INAF/IASF Milano, Via E. Bassini 15, Milano, Italy
[46] INFN, Sezione di Bologna, Via Irnerio 46, I-40126, Bologna, Italy
[47] INFN, Sezione di Roma 1, Università di Roma Sapienza, Piazzale Aldo Moro 2, 00185, Roma, Italy
[48] IPAG: Institut de Planétologie et d'Astrophysique de Grenoble, Université Joseph Fourier, Grenoble 1 / CNRS-INSU, UMR 5274, Grenoble, F-38041, France
[49] IUCAA, Post Bag 4, Ganeshkhind, Pune University Campus, Pune 411 007, India
[50] Imperial College London, Astrophysics group, Blackett Laboratory, Prince Consort Road, London, SW7 2AZ, U.K.
[51] Infrared Processing and Analysis Center, California Institute of Technology, Pasadena, CA 91125, U.S.A.
[52] Institut Néel, CNRS, Université Joseph Fourier Grenoble I, 25 rue des Martyrs, Grenoble, France
[53] Institut Universitaire de France, 103, bd Saint-Michel, 75005, Paris, France
[54] Institut d'Astrophysique Spatiale, CNRS (UMR8617) Université Paris-Sud 11, Bâtiment 121, Orsay, France
[55] Institut d'Astrophysique de Paris, CNRS (UMR7095), 98 bis Boulevard Arago, F-75014, Paris, France
[56] Institute for Space Sciences, Bucharest-Magurale, Romania
[57] Institute of Astronomy and Astrophysics, Academia Sinica, Taipei, Taiwan
[58] Institute of Astronomy, University of Cambridge, Madingley Road, Cambridge CB3 0HA, U.K.
[59] Institute of Theoretical Astrophysics, University of Oslo, Blindern, Oslo, Norway
[60] Instituto de Física de Cantabria (CSIC-Universidad de Cantabria), Avda. de los Castros s/n, Santander, Spain
[61] Jet Propulsion Laboratory, California Institute of Technology, 4800 Oak Grove Drive, Pasadena, California, U.S.A.
[62] Jodrell Bank Centre for Astrophysics, Alan Turing Building, School of Physics and Astronomy, The University of Manchester, Oxford Road, Manchester, M13 9PL, U.K.
[63] Kavli Institute for Cosmology Cambridge, Madingley Road, Cambridge, CB3 0HA, U.K.
[64] LAL, Université Paris-Sud, CNRS/IN2P3, Orsay, France
[65] LERMA, CNRS, Observatoire de Paris, 61 Avenue de l'Observatoire, Paris, France
[66] Laboratoire AIM, IRFU/Service d'Astrophysique - CEA/DSM - CNRS - Université Paris Diderot, Bât. 709, CEA-Saclay, F-91191 Gif-sur-Yvette Cedex, France
[67] Laboratoire Traitement et Communication de l'Information, CNRS (UMR 5141) and Télécom ParisTech, 46 rue Barrault F-75634 Paris Cedex 13, France
[68] Laboratoire de Physique Subatomique et de Cosmologie, Université Joseph Fourier Grenoble I, CNRS/IN2P3, Institut National Polytechnique de Grenoble, 53 rue des Martyrs, 38026 Grenoble cedex, France
[69] Laboratoire de Physique Théorique, Université Paris-Sud 11 & CNRS, Bâtiment 210, 91405 Orsay, France
[70] Lawrence Berkeley National Laboratory, Berkeley, California, U.S.A.
[71] Max-Planck-Institut für Astrophysik, Karl-Schwarzschild-Str. 1, 85741 Garching, Germany
[72] McGill Physics, Ernest Rutherford Physics Building, McGill University, 3600 rue University, Montréal, QC, H3A 2T8, Canada
[73] National University of Ireland, Department of Experimental Physics, Maynooth, Co. Kildare, Ireland
[74] Niels Bohr Institute, Blegdamsvej 17, Copenhagen, Denmark
[75] Observational Cosmology, Mail Stop 367-17, California Institute of Technology, Pasadena, CA, 91125, U.S.A.
[76] Optical Science Laboratory, University College London, Gower Street, London, U.K.
[77] SB-ITP-LPPC, EPFL, CH-1015, Lausanne, Switzerland
[78] SISSA, Astrophysics Sector, via Bonomea 265, 34136, Trieste, Italy
[79] School of Physics and Astronomy, Cardiff University, Queens Buildings, The Parade, Cardiff, CF24 3AA, U.K.
[80] Space Sciences Laboratory, University of California, Berkeley, California, U.S.A.
[81] Special Astrophysical Observatory, Russian Academy of Sciences, Nizhnij Arkhyz, Zelenchukskiy region, Karachai-Cherkessian Republic, 369167, Russia
[82] Stanford University, Dept of Physics, Varian Physics Bldg, 382 Via Pueblo Mall, Stanford, California, U.S.A.
[83] Sub-Department of Astrophysics, University of Oxford, Keble Road, Oxford OX1 3RH, U.K.
[84] Theory Division, PH-TH, CERN, CH-1211, Geneva 23, Switzerland
[85] UPMC Univ Paris 06, UMR7095, 98 bis Boulevard Arago, F-75014, Paris, France
[86] Université de Toulouse, UPS-OMP, IRAP, F-31028 Toulouse cedex 4, France
[87] University of Granada, Departamento de Física Teórica y del Cosmos, Facultad de Ciencias, Granada, Spain
[88] University of Miami, Knight Physics Building, 1320 Campo Sano Dr., Coral Gables, Florida, U.S.A.
[89] Warsaw University Observatory, Aleje Ujazdowskie 4, 00-478 Warszawa, Poland